



Contents lists available at ScienceDirect

Remote Sensing of Environment

journal homepage: www.elsevier.com/locate/rse

A three-step semi analytical algorithm (3SAA) for estimating inherent optical properties over oceanic, coastal, and inland waters from remote sensing reflectance

Daniel S.F. Jorge^{a,*}, Hubert Loisel^{a,*}, Cédric Jamet^a, David Dessailly^b, Julien Demaria^c, Annick Bricaud^d, Stéphane Maritorena^e, Xiaodong Zhang^f, David Antoine^{d,g}, Tiit Kutser^h, Simon Bélangerⁱ, Vittorio O. Brando^j, Jeremy Werdell^k, Ewa Kwiatkowska^b, Antoine Mangin^c, Odile Fanton d'Andon^c

^a Univ. Littoral Côte d'Opale, CNRS, Univ. Lille, UMR 8187 - LOG - Laboratoire d'Océanologie et de Géosciences, F-62930 Wimereux, France

^b EUMETSAT, Darmstadt, Germany

^c ACRI-ST, Sophia Antipolis Cedex 06904, France

^d Sorbonne Université, CNRS, Laboratoire d'Océanographie de Villefranche, LOV, Villefranche-sur-Mer, France

^e Earth Research Institute, University of California Santa Barbara, Santa Barbara, CA 93106, USA

^f Division of Marine Science, School of Ocean Science and Engineering, The University of Southern Mississippi, Stennis Space Center, MS 39529, USA

^g Remote Sensing and Satellite Research Group, School of Earth and Planetary Sciences, Curtin University, Perth, WA 6845, Australia

^h Estonian Marine Institute, University of Tartu, Estonia

ⁱ Département de Biologie, Chimie et Géographie and BORÉAS, Université du Québec à Rimouski, Canada

^j Institute of Marine Sciences, National Research Council of Italy (CNR-ISMAR), Rome, Italy

^k NASA Goddard Space Flight Center, Greenbelt, MD 20771, USA

ARTICLE INFO

Editor: Menghua Wang

ABSTRACT

We present a three-step inverse model (3SAA) for estimating the inherent optical properties (IOPs) of surface waters from the remote sensing reflectance spectra, $R_{rs}(\lambda)$. The derived IOPs include the total ($a(\lambda)$), phytoplankton ($a_{phy}(\lambda)$), and colored detrital matter ($a_{cdm}(\lambda)$), absorption coefficients, and the total ($b_b(\lambda)$) and particulate ($b_{bp}(\lambda)$) backscattering coefficients. The first step uses an improved neural network approach to estimate the diffuse attenuation coefficient of downwelling irradiance from R_{rs} . $a(\lambda)$ and $b_{bp}(\lambda)$ are then estimated using the LS2 model (Loisel et al., 2018), which does not require spectral assumptions on IOPs and hence can assess $a(\lambda)$ and $b_b(\lambda)$ at any wavelength at which $R_{rs}(\lambda)$ is measured. Then, an inverse optimization algorithm is combined with an optical water class (OWC) approach to assess $a_{phy}(\lambda)$ and $a_{cdm}(\lambda)$ from $a_{nw}(\lambda)$. The proposed model is evaluated using an in situ dataset collected in open oceanic, coastal, and inland waters. Comparisons with other standard semi-analytical algorithms (QAA and GSM), as well as match-up exercises, have also been performed. The applicability of the algorithm on OLCI observations was assessed through the analysis of global IOPs spatial patterns derived from 3SAA and GSM. The good performance of 3SAA is manifested by median absolute percentage differences (MAPD) of 13%, 23%, 34% and 34% for $b_{bp}(443)$, $a_{nw}(443)$, $a_{phy}(443)$ and $a_{cdm}(443)$, respectively for oceanic waters. Due to the absence of spectral constraints on IOPs in the inversion of total IOPs, and the adoption of an OWC-based approach, the performance of 3SAA is only slightly degraded in bio-optical complex inland waters.

1. Introduction

A great effort has been made in the last decades to develop and improve the estimation of inherent optical properties (IOPs) of surface

natural waters from satellite ocean color radiometry (OCR) observations (IOCCG, 2006; Werdell et al., 2018). While many studies focused on open ocean Case 1 waters (Morel and Prieur, 1977) where IOPs are largely driven by phytoplankton and its by-products, there are emerging

* Corresponding authors.

E-mail addresses: daniel.jorge@univ-littoral.fr (D.S.F. Jorge), hubert.loisel@univ-littoral.fr (H. Loisel).

<https://doi.org/10.1016/j.rse.2021.112537>

Received 16 September 2020; Received in revised form 14 May 2021; Accepted 25 May 2021

Available online 17 June 2021

0034-4257/© 2021 The Authors.

Published by Elsevier Inc.

This is an open access article under the CC BY-NC-ND license

(<http://creativecommons.org/licenses/by-nc-nd/4.0/>).

needs for deriving IOPs in Case 2 optically complex waters which are more commonly encountered in coastal and inland aquatic environments. Interest in IOPs and their derivation from OCR stems from their role in the propagation of light in water, which in turn affects light-associated processes such as primary production, visibility, and phytoplankton diel vertical migration. The sensitivity of IOPs to the variability of optically significant components (OSC) also allows IOPs to be used as proxies of various seawater dissolved and particulate constituents of biogeochemical significance. For instance, the particulate backscattering coefficient, b_{bp} , has long been used as a proxy of particulate organic carbon in open ocean waters (Stramski et al., 1999; Loisel et al., 2002; Duforêt-Gaurier et al., 2010; Cetinić et al., 2012), or of suspended particulate matter in coastal waters (Neukermans et al., 2012; Balasubramanian et al., 2020). Similarly, absorption by colored dissolved organic matter and its spectral behavior, especially in the UV, allows the variability of dissolved organic carbon to be assessed in coastal waters (Ferrari, 2000; Mannino et al., 2008; Vantrepotte et al., 2015).

The total absorption ($a(\lambda)$) and backscattering ($b_b(\lambda)$) coefficients (both in units of m^{-1} , and λ representing the wavelength of light in vacuum in units of nm) can be expressed as the sum of the contributions from each OSC including pure seawater. For instance, $a(\lambda)$ is contributed by the absorption by water molecules including dissolved salts ($a_w(\lambda)$), phytoplankton cells ($a_{phy}(\lambda)$), non-algal particles, including heterotrophic bacteria, detritus, and mineral particles ($a_{nap}(\lambda)$), and colored dissolved organic matter ($a_{cdm}(\lambda)$). The latter two absorption coefficients have similar spectral shapes and are usually summed together to form the absorption of colored dissolved plus detrital matter ($a_{cdm}(\lambda) = a_{nap}(\lambda) + a_{cdm}(\lambda)$). Similarly, $b_b(\lambda)$ is the sum of backscattering by pure seawater ($b_{bw}(\lambda)$), and suspended particles ($b_{bp}(\lambda)$). At first order the IOPs variability is driven by the concentration of OSC and, at second order, by the chemical nature of dissolved organic matter, and size distribution, shape, heterogeneity, and chemical composition of particulate matter.

Several semi-analytical algorithms (SAA) are now available to estimate the different IOPs from the remote sensing reflectance, $R_{rs}(\lambda)$. They can be divided into two categories following a bottom-up or a top-down strategy (Mouw et al., 2015). For the top-down algorithms, such as QAA (Lee et al., 2002), the total absorption and backscattering coefficients are estimated first. For the bottom-up algorithms the component IOPs (i. e., $a_{phy}(\lambda)$, $a_{cdm}(\lambda)$ and $b_{bp}(\lambda)$) are first retrieved using an optimization procedure before being summed up with the water IOPs to derive the total IOPs (Garver and Siegel, 1997; Maritorea et al., 2002; Lee et al., 1994; Lee et al., 1999, 2002; Doerffer and Fischer, 1994; Werdell et al., 2013). In either of these two categories of SAA, spectral shape functions, often referred to as eigenvectors (but not only), have to be assumed for each considered IOP.

An exception is the LS model (Loisel and Stramski, 2000; Loisel et al., 2001) and its recently improved version (Loisel et al., 2018), LS2, which are based on statistical relationships between $R_{rs}(\lambda)$ and IOPs and make no assumption on the spectral shape of $a(\lambda)$ and $b_b(\lambda)$. Either LS or LS2 requires two inputs, which are $R_{rs}(\lambda)$ and the average attenuation coefficient ($\langle K_d(\lambda) \rangle_1$), for downwelling irradiance within the first attenuation depth. For satellite remote sensing applications, $\langle K_d(\lambda) \rangle_1$ is estimated from $R_{rs}(\lambda)$ using a neural network approach (Jamet et al., 2012; Loisel et al., 2018). Note that although no spectral assumptions on IOP are made in LS or LS2, there might be some spectral constraints inherent in the training data for developing the neural network to estimate $\langle K_d(\lambda) \rangle_1$ from $R_{rs}(\lambda)$. One of the advantage of the LS or LS2 model is that the spectral slope of $b_{bp}(\lambda)$ can be retrieved from $b_{bp}(\lambda)$, independently derived at several wavelengths (Loisel et al., 2006), which can then be used to assess information about the particle size distribution (Kostadinov et al., 2009, 2010). From the non-water absorption coefficient, $a_{nw}(\lambda)$, which can be estimated at each visible wavelength independently, the different sub-components such as $a_{phy}(\lambda)$ and $a_{cdm}(\lambda)$ can be calculated using various models (Ciotti and Bricaud, 2006; Zheng and Stramski, 2013; and Zhang et al., 2015). This

procedure, following a top-down strategy, may be more sensitive to $R_{rs}(\lambda)$ noise propagation in contrast to bottom-up models that use optimization procedures. However, in the bottom-up strategy, the inherent uncertainty associated with $a(\lambda)$ or $b_b(\lambda)$ retrieval may be wrongly compensated to the other when these two IOPs are simultaneously estimated during the optimization process. Besides, in the one-step algorithms, or bottom-up strategy, the final solution is tightly constrained by the adopted eigenvectors.

The objective of this paper is to develop a methodology aiming at estimating $a_{nw}(\lambda)$, $b_{bp}(\lambda)$, $a_{cdm}(\lambda)$, and $a_{phy}(\lambda)$ from OCR observations over open, coastal, and inland waters. For that purpose, a slightly modified version of the LS2 model is combined with an adapted version of the Zhang et al. (2015) algorithm accounting for some bio-optical specificities through the use of optical water classes (OWC). This method, hereafter referred to as Three-step Semi Analytical Algorithm (3SAA), is tested using different in situ and satellite datasets that are first presented. Then the structure of 3SAA and its validation using these datasets and per OWC are provided. The performance of 3SAA is also compared to those obtained from the QAA (Lee et al., 2002) and GSM (Maritorea et al., 2002) algorithms using monthly *Ocean and Land Color Instrument (OLCI)* data.

2. Data and methods

2.1. The validation datasets

The 3SAA algorithm is evaluated using four independent datasets. The first two datasets are composed of in situ $R_{rs}(\lambda)$ and IOPs, with the first measured in marine waters (DS-MW) and the second in coastal ocean and inland waters (DS-IW). The third (DS-Sat) and fourth (DS-Argo) validation datasets are both composed of in situ IOPs and co-located and nearly simultaneous satellite $R_{rs}(\lambda)$. The spatial distribution of each dataset can be seen in Fig. 1. Following the turbidity flag developed by Robinson et al. (2003) which assumes that waters with $R_{rs}(670)$ higher than 0.0012 sr^{-1} are considered as turbid, the four datasets cover a variable fraction of turbid waters: 4.3%(DS-MW), 88%(DS-IW), 4.7%(DS-Sat), and 0%(DS-Argo).

2.1.1. In situ IOPs in open ocean and coastal waters (DS-MW)

This dataset includes in situ data collected in various environments that have been presented in Loisel et al. (2018) and Valente et al. (2016), and those collected (and not gathered in Valente et al. (2016)) in the frame of the BOUSSOLE (Antoine et al., 2006), Plumes and Blooms (Kostadinov et al., 2012), and PEACETIME projects (J. Uitz, E. Boss and N. Haëntjens, contribution to the “PEACETIME-OC” project funded by CNES). The IOPs values in DS-MW cover a broad range of variability (Fig. 2). The larger number of b_{bp} data points is contributed by the BOUSSOLE (Antoine et al., 2006) dataset in which b_{bp} has been measured by an automatic system every 15 min between 08:00 AM and 04:00 PM since May 2015. For match-up, only the ones from the daily continuous- measurements in the BOUSSOLE and PEACETIME-OC that were close to the satellite overpass were kept.

2.1.2. In situ IOPs in inland waters (DS-IW)

The dataset for inland waters (DS-IW) is composed of measurements collected in optically complex lakes and rivers by different research groups in Canada (Binding et al., 2018; Bélanger et al., 2017), the United States (Mouw et al., 2017; Casey et al., 2020), Brazil (Jorge et al., 2017), Estonia (Kutser et al., 2016) and the Netherlands (Spyrakos et al., 2018). Even though the number of data points in DS-IW is much lower than in DS-MW, DS-IW still covers significant variability (Fig. 3).

2.1.3. Satellite-to-in situ matchup datasets (DS-Sat and DS-Argo)

DS-Sat (Fig. 4) includes in situ IOPs measurements collected during oceanographic cruises and from the fixed buoy, BOUSSOLE (Antoine et al., 2006) from September of 1997 to November of 2017, and

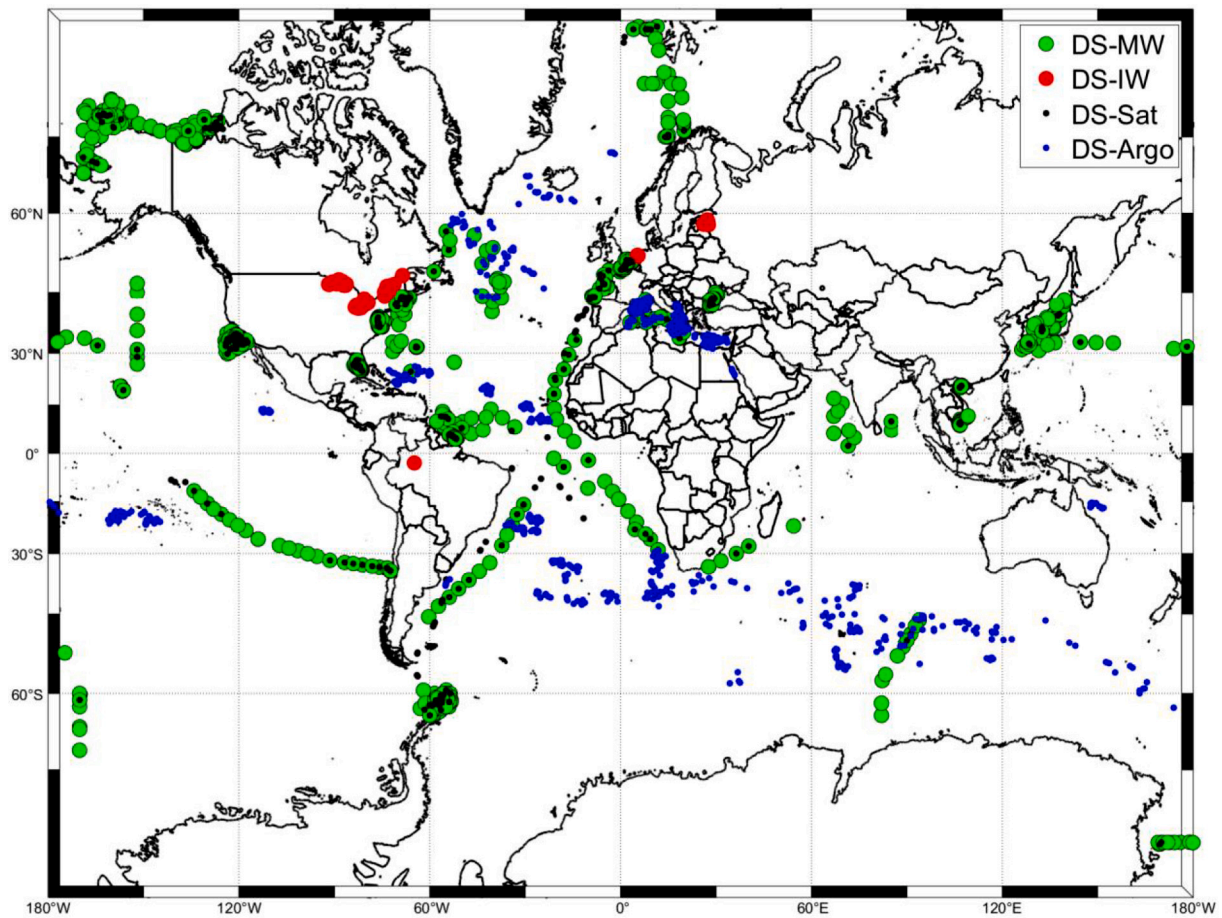


Fig. 1. Distribution of the four validation datasets as indicated: In situ marine waters (DS-MW), Inland waters (DS-IW); Match-up dataset (DS-Sat); Match-up dataset using biogeochemical Argo floats (DS-Argo).

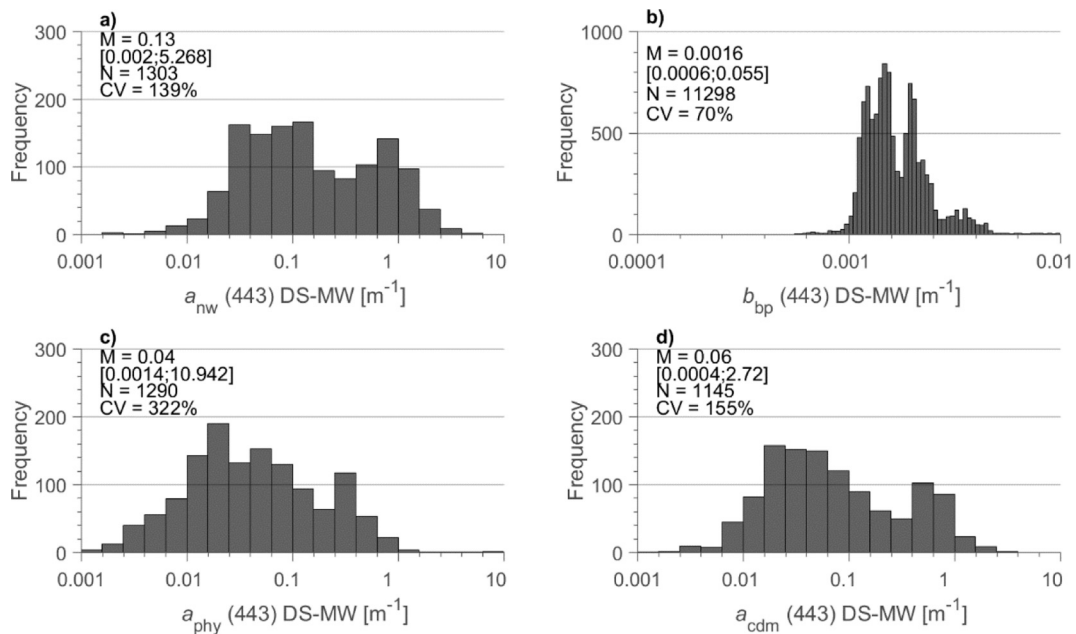


Fig. 2. Histograms and relevant statistical parameters of $a_{nw}(443)$, $b_{bp}(443)$, $a_{phy}(443)$, and $a_{cdm}(443)$ for the DS-MW dataset. M, N, and CV stand for median value, number of data points, and coefficient of variation, respectively. The minimum-to-maximum range values for the optical coefficients are indicated between bracket.

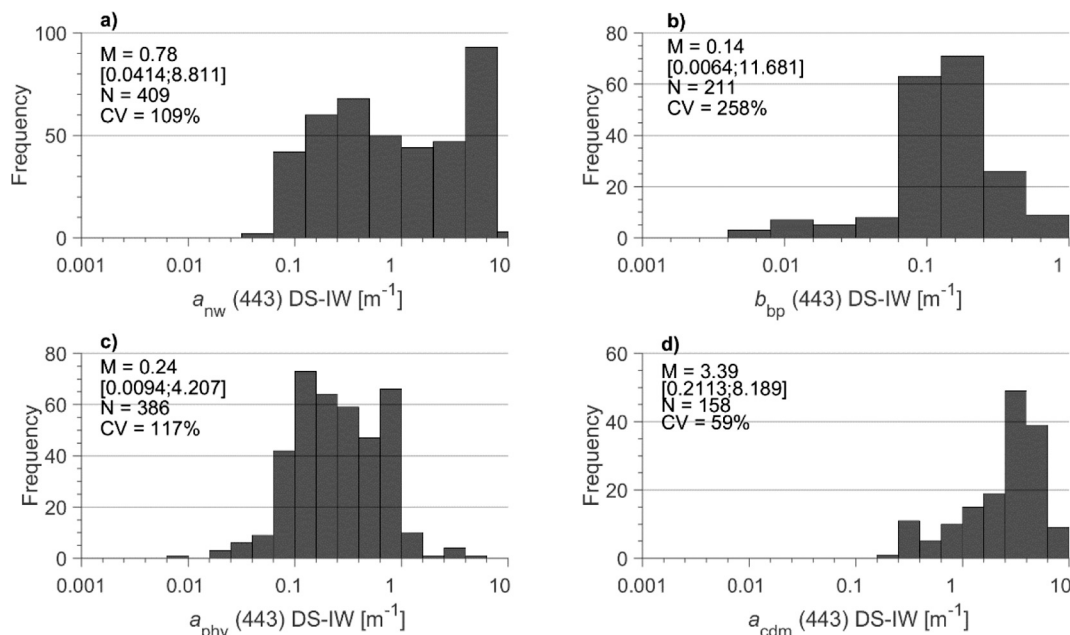


Fig. 3. Same as Fig. 2 but for DS-IW.

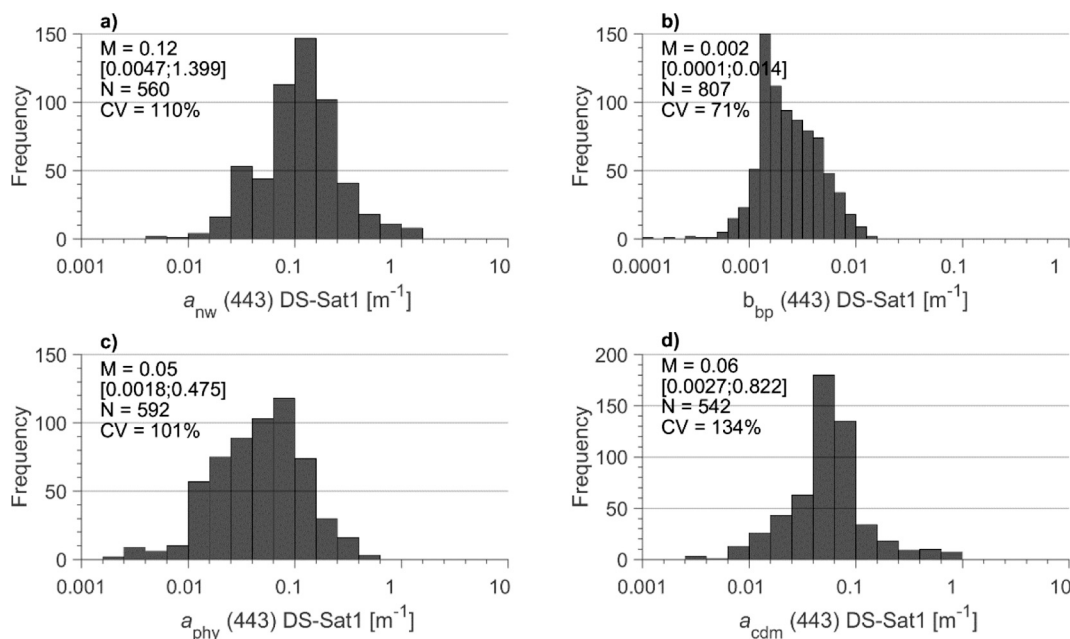


Fig. 4. Same as Fig. 2 but for DS-Sat.

GlobColour $R_{rs}(\lambda)$ products merged from different sensors (http://www.globcolour.info/CDR_Docs/GlobCOLOUR_PUG.pdf), including the Medium Resolution Imaging Spectrometer (MERIS), the Moderate-Resolution Imaging Spectroradiometer (MODIS), the Sea-viewing Wide Field-of-view Sensor (SeaWiFS) and the Visible Infrared Imaging Radiometer Suite (VIIRS). Being a merged product, the GlobColour data ensure a higher coverage than that available from single sensor products, and then a higher number of match-up data points, but within a time window that can be as large as 12 h.

DS-Argo (Fig. 4) is exclusively composed of in situ $b_{bp}(700)$ measurements collected between 04/2016 and 09/2018 by autonomous profiling floats from the biogeochemical Argo (BGC-Argo) network (Claustre et al., 2020) and the matched OLCI $R_{rs}(\lambda)$ data. The use BGC-Argo dataset increases considerably the number of match-up data

points, as shown in Bisson et al. (2019).

We used the MERMAID tools protocol (<http://mermaid.acri.fr/data/proto/dataproto.php>), which is in turn based on the NASA Ocean Color protocol (Bailey and Wang, 2001) to match satellite data with IOPs for DS-Sat and DS-Argo datasets. Basically, matchup was performed within a 3×3 pixel window, in which the coefficient of variation of R_{rs} needs to be below 0.1 for each wavelength and the number of valid pixels needs to be at least 5. These two different match-up datasets allow the model to be evaluated accounting for uncertainties associated with atmospheric corrections as well as those related to match-up exercises such as the spatio-temporal mismatch between in situ sampling and satellite overpass.

Compared to the in situ datasets, the number of data points in DS-Sat is considerably lower, although high enough to have a global

distribution and a 4-order range of variability, allowing the model to be properly evaluated from satellite data (Fig. 4).

2.2. The QAA and GSM models

The performance of the 3SAA algorithm is compared with the results obtained using the GSM model (Maritorena et al., 2010) implemented in GlobColour (GlobColour, 2020) or the QAA algorithm (v6; Lee et al., 2002; Lee et al., 2014). In this version of GSM (hereafter referred to as GSM-GC), the spectral slopes of a_{cdm} and b_{bp} are set to 0.02061 nm^{-1} and 1.03373 , respectively as in Maritorena et al. (2002), but a weighting function is used during the optimization. The specific phytoplankton absorption values are from Maritorena et al. (2002). In QAA v6 obtained from the Ocean Color platform (https://oceancolor.gsfc.nasa.gov/doc/s/ocssw/qaa_8c.html), the spectral slopes of a_{cdm} (Y_{cdm}) and b_{bp} (Y_{bbp}) are calculated as follows:

$$Y_{cdm} = 0.015 + \left(\frac{0.002}{0.6 + r_{rs}(443)/r_{rs}(560)} \right) \quad (1)$$

$$Y_{bbp} = 2 \left(1 - 1.2 \exp \left(-0.9 \frac{r_{rs}(443)}{r_{rs}(560)} \right) \right) \quad (2)$$

where r_{rs} is the remote sensing reflectance just below the surface and is linked to R_{rs} as $r_{rs} = R_{rs}/(0.52 + 1.7 R_{rs})$. For both GSM and QAA, the same pure water absorption, a_w and backscattering b_{bw} , coefficients values are used, and are estimated from Mason et al. (2016) and Zhang et al. (2009), respectively.

2.3. Description of the 3SAA algorithm

The general workflow of the 3SAA algorithm can be divided into seven sub-steps (Table 1). a_{nw} and b_{bp} are estimated using the Loisel et al. (2018) algorithm in sub-steps 1 to 5, in which $\langle K_d \rangle_1$ is estimated as the first step using a neural network approach with R_{rs} and μ_w as input, and a_{nw} and b_{bp} are subsequently estimated as the second step. Lastly, a_{cdm} and a_{phy} are estimated as the third step following the sub-steps 6 and 7, based on the algorithm of Zhang et al. (2015) with slight modifications to account for the optical specificity of the water masses through the use of optical water classes (OWC) (Mélin and Vantrepotte, 2015). Mélin and Vantrepotte (2015) defined sixteen OWC and we added an additional 17th optical class to account for ultra-oligotrophic waters from the South Pacific gyre. For partitioning $a_{nw}(\lambda)$ into $a_{cdm}(\lambda)$ and $a_{phy}(\lambda)$, the model of Zhang et al. (2015) has been preferred to those of Ciotti and Bricaud (2006) and Zheng and Stramski (2013) due to its general applicability which allows much higher number of retrieved data points to be estimated and better accuracy.

The LS2 model was developed from radiative transfer simulations to estimate the total absorption ($a(\lambda)$), and backscattering ($b_b(\lambda)$), coefficients within the surface ocean, from the remote sensing reflectance ($R_{rs}(\lambda)$), and the average attenuation coefficient for downwelling irradiance ($\langle K_d \rangle_1$ (m^{-1})). To better address the transition from oligotrophic to turbid waters, the neural net (NN) used to estimate $\langle K_d \rangle_1$ optionally uses the red part of the spectrum (i. e. 670 nm) depending on the trophic status of the water body (see discussion in Loisel et al., 2018). A validation exercise performed with in situ $\langle K_d \rangle_1$ measurements has shown that this NN is able to estimate $\langle K_d \rangle_1$ with a MAPD value around 21% at all wavelengths, except at 412 nm where MAPD reached 27% (see Fig. 5 in Loisel et al., 2018). For 3SAA, this neural network has been improved to account for the effect of the sun angle on the $\langle K_d \rangle_1$ variability (Kirk, 1984; Gordon, 1989, and Morel and Loisel, 1998), using μ_w as an additional input to the NN, which estimates $\langle K_d \rangle_1$ at any wavelengths between 400 and 700 nm. For $R_{rs}(490)/R_{rs}(555) < 0.85$ (see Zhang and Fell, 2007), the NN has two hidden layers with 9 neurons on the first hidden layer and 6 on the second hidden layer. For

Table 1

The Logical Flow of the 3SAA Inverse Reflectance Model which uses $R_{rs}(\lambda)$ in the visible part of the spectrum and the sun zenith angle, θ , as inputs of the model.

Sub-steps	Description of each sub-step of the model
Sub-step 1	μ_w is calculated as $\mu_w = \cos[\sin^{-1}(\sin(\theta)/n_w)]$, where μ_w is the cosine of the angle of refraction of the solar beam just beneath the sea surface, n_w is the refractive index of sea water with $n_w = 1.34$ (n_w can also be calculated using Zhang et al., 2009 as a function of the temperature and Salinity when available).
Sub-step 2	$\langle K_d \rangle_1$ is obtained from a neural network algorithm (described in this paper), which required R_{rs} as input parameter (in this case the inversion of $\langle K_d \rangle_1$ at one given wavelength, requires R_{rs} at several visible wavelengths) and μ_w .
Sub-step 3	Chl-a is estimated from the OC4v6 algorithm (O'Reilly et al., 2000) and is used only as an initial guess in an iterative process to calculate $\eta = b_w(\lambda)/b(\lambda)$ as fully described in Loisel et al. (2018). Pure sea water backscattering ($b_{bw}(\lambda)$), and absorption ($a_w(\lambda)$), coefficients are calculated according to Zhang et al. (2009) and Mason et al. (2016), respectively. The implementation of the temperature and salinity dependence of $b_{bw}(\lambda)$ is done following Werdell et al. (2013) for image processing, and the in situ T and S measurements are used for the validation exercises.
Sub-step 4	The total absorption ($a(\lambda)$), and backscattering ($b_b(\lambda)$), coefficients are then calculated from LS2 (Loisel et al., 2018) (involving the correction of Raman scattering through the iterative process described in Loisel et al., 2018).
Sub-step 5	The non-water absorption coefficient ($a_{nw}(\lambda)$), and the particulate backscattering coefficient ($b_{bp}(\lambda)$), are then obtained by subtracting $a_w(\lambda)$ and $b_{bw}(\lambda)$ from $a(\lambda)$ and $b_b(\lambda)$, respectively.
Sub-step 6	The optical water class (OWC) of a given pixel is estimated from the $R_{rs}(\lambda)$ visible spectrum following Mélin and Vantrepotte (2015). These OWC have been generated from SeaWiFS global $R_{rs}(\lambda)$ data using an unsupervised clustering technique applied to normalized $R_{rs}(\lambda)$ spectra to attenuate the impact of the change of concentration of OSC on OWC (Lubac and Loisel, 2007). Despite this dataset, used to calibrate the 17 OWC, having been collected over global coastal waters (but including the Mediterranean Sea), it covers almost all kind of optical conditions from very turbid to oligotrophic waters. Based on a comparison exercise performed using a standard Case 1 bio-optical model (Morel and Maritorena, 2001) Mélin and Vantrepotte (2015) showed that spectra belonging to classes 9 to 16 can be classified as mesotrophic to oligotrophic Case-1 waters spectra ($\text{Chl-a} < 0.4 \text{ mg.m}^{-3}$). The other remaining OWC present $R_{rs}(\lambda)$ spectral shapes that depart from those described by a Case-1 model and will be addressed in sub-step 7. For the present study, an additional 17th class was added to account for ultra-oligotrophic waters allowing the global ocean to be fully covered by these 17 OWC (not shown).
Sub-step 7	The estimation of $a_{phy}(\lambda)$ and $a_{cdm}(\lambda)$ from $a_{nw}(\lambda)$ is performed for each optical water class using the algorithm of Zhang et al. (2015). <ul style="list-style-type: none"> a- For optically complex waters (OWC 1 and 2), the algorithm uses the full Zhang et al. (2015) optimization techniques to retrieve Y_{cdm}, $a_{cdm}(\lambda)$, and $a_{phy}(\lambda)$ with $a_{nw}(\lambda)$ at 412, 443, 490 and 510 nm as input. b- For OWC between 3 and 14, Y_{cdm} is estimated using Eq. 3. The estimated Y_{cdm} and $a_{nw}(\lambda)$ at 412, 443, 490 and 510 nm were used as input to Zhang et al. (2015) model to retrieve $a_{phy}(\lambda)$ and $a_{cdm}(\lambda)$: $Y_{cdm} = 0.019 + \left(\frac{0.002}{0.6 + r_{rs}(443)/r_{rs}(560)} \right) \quad (3)$ c- For the 15th or higher (clear waters) OWC, the Y_{cdm} is retrieved following Eq. 3, and the three a_{phy}^* spectra in Zhang et al. (2015) were replaced with three a_{phy}^* reference spectra from Bricaud et al. (2010).

$R_{rs}(490)/R_{rs}(555) \geq 0.85$, the NN has two hidden layers with 8 neurons on the first hidden layer and 6 on the second hidden layer. Using μ_w as an input parameter to the NN improves the estimation of $\langle K_d \rangle_1$ (Fig. 6). The residual dependence of $\langle K_d \rangle_1$ calculated using LS on the Sun zenith angle, especially at low $\langle K_d \rangle_1$ values (Fig. 6a) disappeared when LS2 is used (Fig. 6b). The same improvement is also observed at other wavelengths (not shown).

The non-water absorption coefficient (a_{nw}), and particulate backscattering (b_{bp}), coefficients are estimated from a and b_b from which the

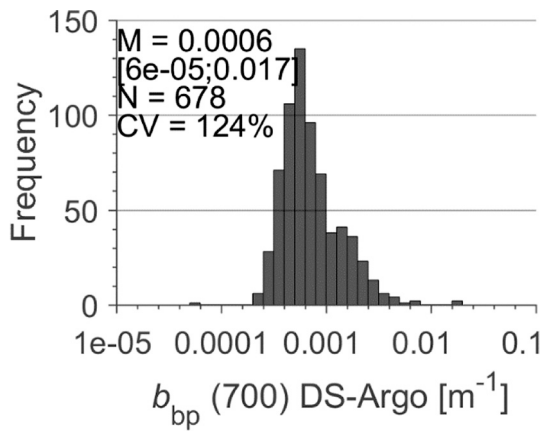


Fig. 5. Same as Fig. 2 but for DS-Argo.

pure sea water absorption and backscattering coefficients are subtracted. The a_w and b_{bw} values are estimated from Mason et al. (2016) and Zhang et al. (2009), respectively. Lee et al. (2015) derived pure sea water absorption coefficients from $R_{rs}(\lambda)$ measurements in very oligotrophic oceanic waters. These values are very similar to Mason et al. (2016) measurements for pure fresh water from 412 nm to longer wavelengths, and could also have been used. The implementation of the temperature and salinity dependence of b_{bw} (Zhang et al., 2009) is done following Werdell et al. (2013).

The third step of 3SAA is based on Zhang et al. (2015) in which $a_{nw}(\lambda)$ is partitioned into $a_{phy}(\lambda)$ and $a_{cdm}(\lambda)$ through an optimization technique using $a_{nw}(\lambda)$ at 412, 443, 490 and 510 nm as input. This model partitions $a_{nw}(\lambda)$ into contributions by three major phytoplankton size classes, micro-, nano- and pico-plankton, each characterized by its own chlorophyll specific a_{phy}^* spectrum (Uitz et al., 2008), and by a fourth component a_{cdm} , parameterized following the standard exponential spectral shape formulation (Bricaud et al., 1981). A water class-based approach is used in 3SAA to increase the performance of the Zhang et al. (2015) algorithm under different conditions. To better account for the optical specificity of water masses, different $a_{phy}^*(\lambda)$ values and approaches used to calculate Y_{cdm} have been adopted (based on sensitivity analysis).

For optically complex waters (OWC 1 and 2), the algorithm uses the full Zhang et al. (2015) optimization techniques to retrieve Y_{cdm} , $a_{cdm}(\lambda)$ and $a_{phy}(\lambda)$. For the OWC 3 to 14, Y_{cdm} is retrieved using Eq. 3, which is based on Lee et al. (2009), and later partitioning into $a_{phy}(\lambda)$ and $a_{cdm}(\lambda)$ is done following Zhang et al. (2015). Because OWC 1 and 2 are

drastically impacted by terrestrial inputs (Mélín and Vantrepotte, 2015), Y_{cdm} cannot be properly estimated from Eq. 3 which was developed from clearer water data in NOMAD. Consequently, OWC 1 & 2 were processed separately.

An over-estimation of $a_{phy}(443)$ in the lower absorption range by the model of Zhang et al. (2015) model was noticed (Fig. 12 in Zhang et al., 2015). To correct for this effect, the Zhang et al. (2015) procedure has been modified for oligotrophic waters. For the OWC 15 to 17 (clear waters), Y_{cdm} is retrieved following Eq. 3, and the three a_{phy}^* reference spectra used in Zhang et al. (2015) model for the other OWC's were updated with measurements collected in the South Pacific Gyre during the BIOSOPE project (Bricaud et al., 2010). Once $a_{cdm}(\lambda)$ is retrieved, $a_{phy}(\lambda)$ is then estimated by subtracting a_{cdm} from a_{nw} . This later step is needed because a_{cdm} largely dominates a_{nw} in the blue in very oligotrophic waters (Bricaud et al., 2010), making the inversion of a_{phy} more sensitive to noise.

2.4. Statistic indicators for model performance

To assess the model performance, we use scatterplots of model predictions vs. observations as well as quantitative statistical metrics of differences between the corresponding model predictions and observations. We calculated several statistical indicators that are typically utilized in the assessment of model accuracy or skill in ocean sciences, including ocean color-related models (e.g., Brewin et al., 2015; Friedrichs et al., 2009; IOCCG, 2006; Stow et al., 2009). These indicators include the root-mean-square deviation (RMSD), calculated in the logarithmic space:

$$RMSD = \left(\frac{\sum_{i=1}^N \left(\log_{10}(IOP_i^{mod}) - (\log_{10}(IOP_i^{obs})) \right)^2}{N - DF} \right)^{0.5} \quad (4)$$

where N is the number of data points, DF is the degrees of freedom (in this case $DF = 2$ and stands for the model-derived and in situ datasets), IOP_i^{mod} represents the model-derived IOP values, and IOP_i^{obs} measured IOP values.

We also report on the median bias (MB), representing the difference between the medians of the model-derived data and corresponding measured data:

$$MB = median(IOP_i^{mod} - IOP_i^{obs}) \quad (5)$$

The median ratio (MR) of model-derived to measured values which provides a non-dimensional measure of bias:

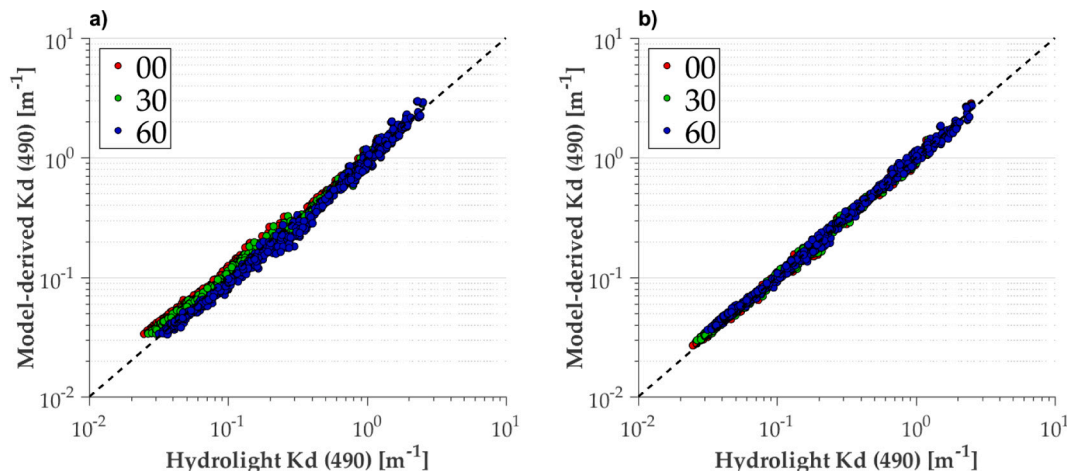


Fig. 6. Comparison of model-derived and reference (true) $\langle K_d(490) \rangle_1$ for the synthetic dataset (IOCCG, 2006) and three sun zenith angles (0° , 30° , 60°) using (a) the model developed in LS2 or (b) the new model.

$$MR = \text{median}\left(\frac{IOP_i^{mod}}{IOP_i^{obs}}\right) \quad (6)$$

The median absolute percent difference (MAPD), is calculated as the median of the individual absolute percent differences between the modeled and measured data:

$$MAPD = \text{median}\left(\frac{|IOP_i^{mod} - IOP_i^{obs}|}{IOP_i^{obs}}\right) * 100 \quad (7)$$

MAPD will also be calculated between IOPs estimated with two different models applied to satellite observations (Section 3.4):

$$MAPD_{sat} = \text{median}\left(\frac{|IOP_i^{mod1} - IOP_i^{mod2}|}{IOP_i^{mod1} + IOP_i^{mod2}}\right) * 200 \quad (8)$$

where IOP_i^{mod1} and IOP_i^{mod2} are the IOPs values estimated from the different models considered.

The other statistic indicators include the Pearson correlation coefficient, r and the slope of the type II linear regression.

3. Results

The 3SAA algorithm allows a_{nw} , b_{bp} , a_{phy} , and a_{cdm} to be estimated from $R_{rs}(\lambda)$ at any wavelength of any multi-spectral spaceborne ocean color sensors (e.g., OLCI). However, the performance of 3SAA is evaluated here at 443 nm, the standard wavelength at which IOPs are delivered by all OCR missions. Besides, we also provide the results for $a_{phy}(665)$, which can be used in coastal and inland waters to infer information about phytoplankton, and which is also at a wavelength less

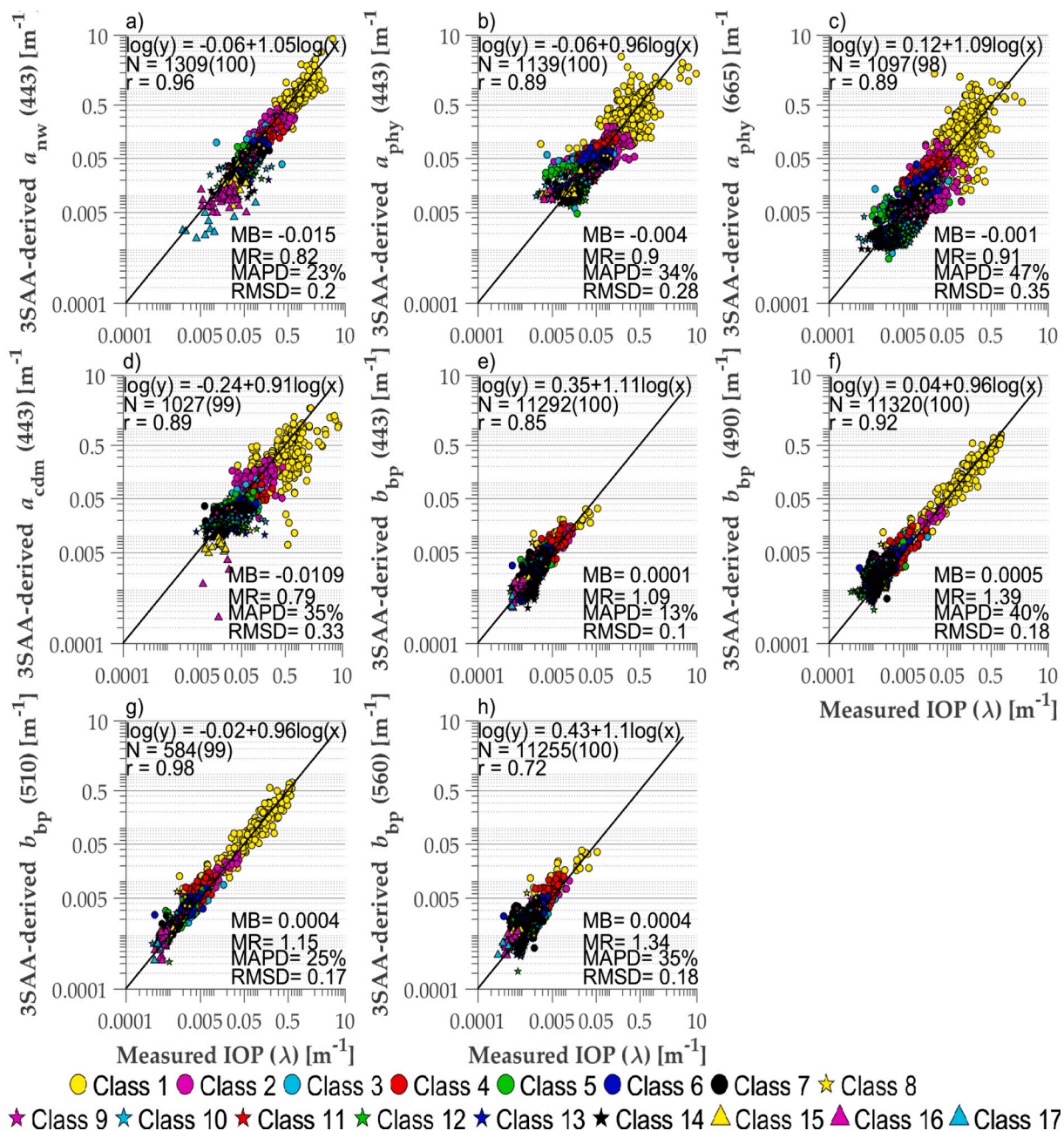


Fig. 7. Comparison of 3SAA-derived and measured values of IOPs for the DS-MW dataset. Each panel is for an IOP at a particular wavelength, as indicated in the y-axis label. The different statistical indicators calculated for the data of 3SAA-derived versus measured IOPs are provided (see text for details). The percentage of retrieved data points is indicated between brackets. The solid line is the 1:1 line. The different colors and shapes stand for a given OWC.

sensitive to packaging effects and accessory pigments than blue wavelengths (Bricaud et al., 1995). Because of the optimization techniques used for partitioning $a_{nw}(\lambda)$ into $a_{phy}(\lambda)$ and $a_{cdm}(\lambda)$, but also of the adopted $a_{phy}^*(\lambda)$ (which here changes according to the OWC), the retrieval of both $a_{phy}(443)$ and $a_{phy}(665)$ are not fully independent (as their retrieval depends on the same 3 eigenvectors). Because LS2 (second step) does not make assumption on the spectral behavior of IOPs and then provides solution at any wavelength, b_{bp} retrievals are also evaluated at 490, 510, and 560 nm. Specific attention is given to the spectral values of b_{bp} , from which the b_{bp} spectral shape can be estimated. This is essentially motivated by the potential use of this slope as a proxy for the particle size distribution, but also because it is as a central constraint in many IOPs algorithms (see discussion in Section 3.2).

3.1. Validation of 3SAA from in situ measurements (DS-MW and DS-IW)

The performance of the 3SAA algorithm is evaluated using the marine (DS-MW) and inland (DS-IW) waters datasets. Over coastal and open ocean waters (DS-MW), we observe a tight correlation between the estimated and measured IOPs (Fig. 7), with no specific behavior according to the considered OWC (Fig. 8). Among the different IOPs at 443 nm, b_{bp} is estimated with the best accuracy (MAPD = 13%), followed by a_{nw} (MAPD = 23%), a_{phy} (MAPD = 34%), and a_{cdm} (MAPD = 35%). The latter two were retrieved with effectively the same accuracy. The MAPD value reaches 47% for $a_{phy}(665)$, but with a relatively low bias (-0.001 m-1). This result was expected due to the usually lower a_{phy} signal in the red compared to the blue. The lower retrieval accuracy observed for a_{phy} and a_{cdm} is due to the propagation of errors from step 2 to step 3, and to errors inherent to step 3. The validation results of the LS2 model used in the second step (i. e. estimation of b_{bp} and a_{nw}), and slightly improved for 3SAA (see Section 2.3), are consistent with the ones published in Loisel et al. (2018). b_{bp} is also retrieved with a relatively good and similar accuracy at the four considered wavelengths, with low bias values (between 2.10^{-4} and 9.10^{-4} m $^{-1}$). The MAPD values are 13%, 40%, 25%, and 35% at 443, 490, 510, and 560 nm, respectively. The lower retrieval accuracy observed at 490 nm compared to the other wavelengths could be explained by the BOUSSOLE dataset for which a net depressing effect in the $b_{bp}(\lambda)$ spectra can be observed at this band (not shown). The same pattern was observed in a recent study in which QAA-v6 was evaluated on the BOUSSOLE dataset, and where the bias (in %) increases by a factor of 1.6 between 443 and 490 nm (Pitarch et al., 2020). Removing this dataset from DS-MW increases the performance of the retrieval at 490 nm by a factor of 1.5 for MAPD (40% to 26%), from 1.39 to 1.11 for MR, and an increase in the determination coefficient

from 0.92 to 0.98. The origin of such pattern (instrument vs. processing) has yet to be identified. The apparently higher values of $b_{bp}(490)$ (Fig. 7f) compared to $b_{bp}(443)$ (Fig. 7e) are simply due to the fact that $b_{bp}(\lambda)$ has not been equally acquired at each band for each station. For instance, $b_{bp}(\lambda)$ is only available at 490 and 510 nm at many stations.

A slight underestimation is observed for all absorption coefficients at 443 nm, which is reflected by the negative bias (-0.015 m $^{-1}$, -0.004 m $^{-1}$ and -0.0109 m $^{-1}$, for $a_{nw}(443)$, $a_{phy}(443)$, and $a_{cdm}(443)$, respectively). In contrast, a slight overestimation is observed for b_{bp} at all wavelengths ($13\% < \text{MAPD} < 40\%$ and $0.0001 < \text{MB} < 0.0005$). A similar behavior has previously been observed by other inverse models tested over the NOMAD dataset (Werdell et al., 2013; Brewin et al., 2015). For instance, in their extensive inter-comparison exercise involving 11 inverse models (Smyth et al., 2006; Devred et al., 2011; Lee et al., 2002; Lee et al., 2009; Lee et al., 1999; Garver and Siegel, 1997; Maritorena et al., 2002; Werdell et al., 2013; Doerffer et al., 2002), Brewin et al. (2015) showed a systematic negative bias for all 11 models for a_{nw} (between -0.05 m $^{-1}$ and -0.0124 m $^{-1}$) and a_{cdm} (between -0.150 m $^{-1}$ and -0.03 m $^{-1}$) and for 10 models for a_{phy} , (between -0.117 m $^{-1}$ and -0.03 m $^{-1}$). The bias for b_{bp} was positive in 9 of the 11 cases, with values ranging from 0.011 to 0.135 for the positive cases, and -0.022 m $^{-1}$ to -0.036 m $^{-1}$ for the negative cases. 3SAA is also able to estimate $a_{phy}(665)$ with a relatively good accuracy (MAPD = 47% and MB = -0.002 m $^{-1}$).

The use of a OWC-based approach greatly improves the performance of the model for the retrieval of $a_{phy}(443)$ (without modifying significantly the $a_{cdm}(443)$ retrieval accuracy). For instance, when the model accounts for OWC-dependent parameters and inversion procedure, instead of using the original Zhang et al. (2015) optimization techniques with the same spectral parameters for every OWC, MB decreases from -0.007 m $^{-1}$ to -0.004 m $^{-1}$, MAPD decreases from 39.7% to 34.2%, and the median ratio increases from 0.78 to 0.9, for the inversion of $a_{phy}(443)$ over the whole validation data set ($N = 1139$). The performance of the model as a function of the optical water class is examined by gathering the 17 OWC into four different groups (Fig. 8). The first group is made of the turbid and absorbing waters (OWC 1 and 2), the second gathers other Case2-waters (OWC 3 to 8), the third group is composed by mesotrophic Case 1 waters (OWC 9 to 12) and the oligotrophic to very-oligotrophic waters (OWC 13 to 17) represent the last group. The MAPD values are relatively similar between the 4 groups, with values between 20 and 37% for $a_{nw}(443)$, 30 and 40% for $a_{phy}(443)$, 30 and 48% for $a_{cdm}(443)$, and 10 and 20% for $b_{bp}(443)$. The highest MAPD values are found for $a_{nw}(443)$ and $a_{cdm}(443)$ over oligotrophic waters and $a_{phy}(443)$ over turbid and absorbing waters.

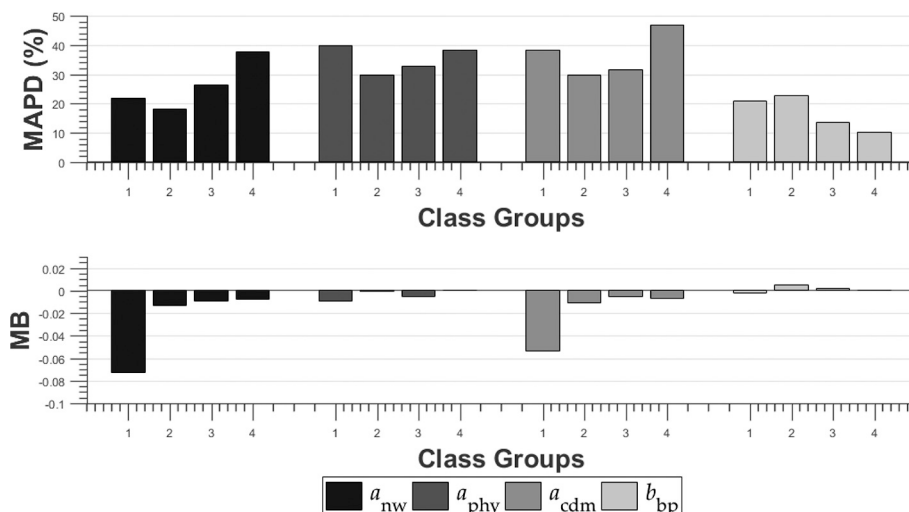


Fig. 8. MAPD and MB (x10 for b_{bp}) values for each IOP at 443 nm. The OWC were grouped as follows: Groups 1 – Classes 1 to 2, Groups 2 – Classes 3 to 8, Groups 3 – Classes 9 to 12, Groups 4 – Classes 13 to 17. Each color represents a different IOP.

Because such result has not been observed for $a_{nw}(\lambda)$ when LS2 was evaluated against synthetic (i.e. error free) data (Loisel et al., 2018), the higher MAPD values for oligotrophic-to-ultra oligotrophic waters is more likely attributable to larger uncertainties in the in situ measurements of $a_{nw}(\lambda)$ in these clear marine environments. In the same way, the lower performance in the estimation of $a_{cdm}(443)$ in oligotrophic waters, also noticed using other inverse models such as GIOPs (Table 4 of Werdell et al., 2013), may partly be associated with the challenging measurements of $a_{cdm}(\lambda)$ in very oligotrophic waters.

$b_{bp}(443)$ is retrieved with the lowest MAPD value (10%) in mesotrophic and oligotrophic waters, and retrieved with relatively low MAPD values (20%) for the two other groups (Case-2 waters). In contrast, MB presents a clear gradient with increasing MB values from group 4 to 1, with larger negative bias being observed for a_{nw} and a_{cdm} in turbid/absorbing water type.

Worsened agreements are expected for inland waters, especially for the third step (Fig. 9), because 3SAA was not initially developed for optically-complex inland waters. The DS-IW dataset mainly covers two OWC (Classes 1 and 2) which were originally identified as very coastal

waters and largely influenced by a large river outflow (Mélain and Van-trepotte, 2015), except for Lake Superior, which have all classes between 1 and 6. The retrieval accuracy for all IOPs is satisfactory (all data points are located around the 1:1 line), but slightly lower than for the coastal and open ocean waters dataset and with some discrepancies according to the considered IOPs. For the absorption coefficients, the best retrieval accuracy is achieved for $a_{nw}(443)$ (MAPD = 29%), $a_{cdm}(443)$ (MAPD = 36%), and $a_{phy}(443)$ (MAPD = 44%).

For the backscattering coefficient, the retrieval accuracy strongly differs according to the inland water sub-dataset considered. For instance, $b_{bp}(443)$ is retrieved with a much better accuracy over the St. Lawrence River and estuary, Canadian lakes, and Lake Superior datasets (MAPD of 23% at 443 nm) than over the Amazonia (MAPD of 83.88% at 443 nm) dataset (Fig. 9). Moreover, in contrast to the Amazonia dataset gathering data from 4 different lakes mainly dominated by organic matter during the sampling period, the quality of the $b_{bp}(\lambda)$ retrieval for the Canadian lakes and Lake Superior data is much higher and does not depend on the wavelength. The complexity of the bulk particulate matter in the Amazonia waters, in situ R_{rs} and IOPs measurements

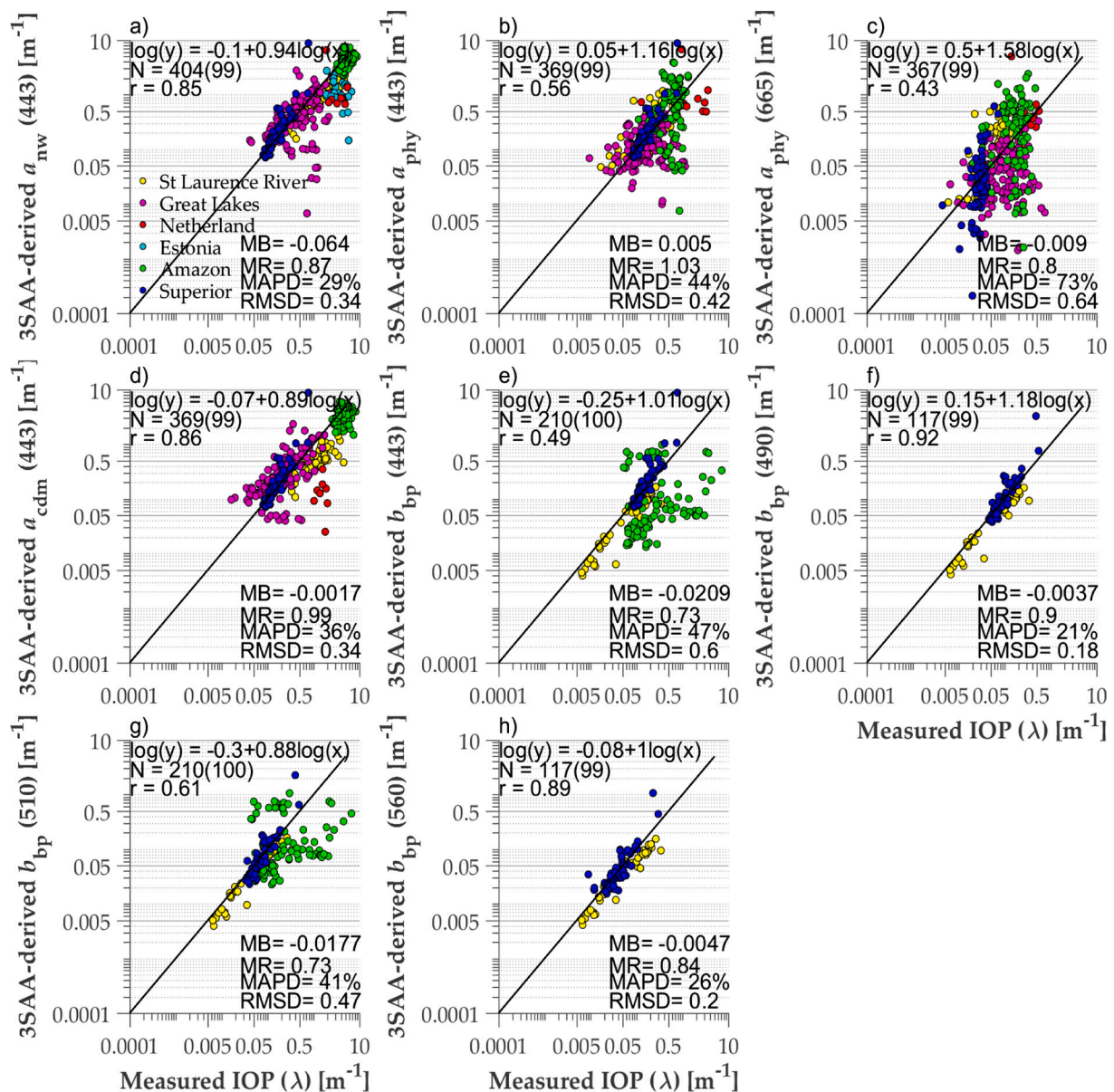


Fig. 9. Comparison of 3SAA-derived and measured values of IOPs for the DS-IW dataset. The different colors stand for the sub datasets used to compose DS-IW, as indicated in the Section 2.1.1.

uncertainties, but also the very high absorption level of these complex waters may explain these patterns (Jorge et al., 2017, Sander de Carvalho et al., 2015). For instance, while the Lake Superior and Amazonia waters have similar $b_{bp}(443)$ values, the Amazonia waters present much higher (about 10 times) $a_{nw}(443)$ values. This relatively high absorption level makes the retrieval of b_{bp} in the blue very challenging for these tropical inland waters (in contrast to Lake Superior waters), as the contribution of $b_{bp}(\lambda)$ to $R_{rs}(\lambda)$ increases, the b_{bp} retrieval significantly improves in the green (MAPD = 72% instead of 84% in the blue; MB = -0.07 m^{-1} instead of -0.16 m^{-1} in the blue) part of the spectrum (unfortunately measurements have not been performed in the red). For such turbid water the correction method proposed by the Hydrosat's manufacturer may not be fully adapted (Doxaran et al., 2016).

The lower retrieval accuracy of $a_{phy}(443)$ observed in inland waters compared with the results obtained in marine waters partly resides into the relative $a_{phy}(443)$ and $a_{cdm}(443)$ range values. For the Amazon

dataset, the median $a_{cdm}(443)$ and $a_{phy}(443)$ values are 4.03 and 0.66 m^{-1} , respectively. In this case, $a_{cdm}(443)$ contributes to more than 85% of $a_{nw}(443)$, making the retrieval of $a_{phy}(443)$ from the $a_{nw}(443)$ spectrum very challenging. This is also true for the whole DS-IW dataset for which the median values of $a_{cdm}(443)$ and $a_{phy}(443)$ are 3.39 m^{-1} , and 0.24 m^{-1} , respectively (Fig. 3). In contrast, the median values of $a_{cdm}(443)$ ($= 0.06 \text{ m}^{-1}$) and $a_{phy}(443)$ ($= 0.04 \text{ m}^{-1}$) in DS-MW are very similar (Fig. 2). This pattern partly explains why a_{phy} and a_{cdm} are retrieved with about the same accuracy for DS-MW, and that a_{cdm} is retrieved with a better accuracy than a_{phy} for DS-IW.

3.2. Performance of 3SAA from match-up exercises (DS-Sat and DS-Argo)

Using the first matchup dataset (DS-Sat), which combines MERIS, SeaWiFS, MODIS and VIIRS images, a good retrieval accuracy is found for all IOPs (Fig. 10). The MAPD (and MB) values for a_{nw} , a_{phy} , a_{cdm} and

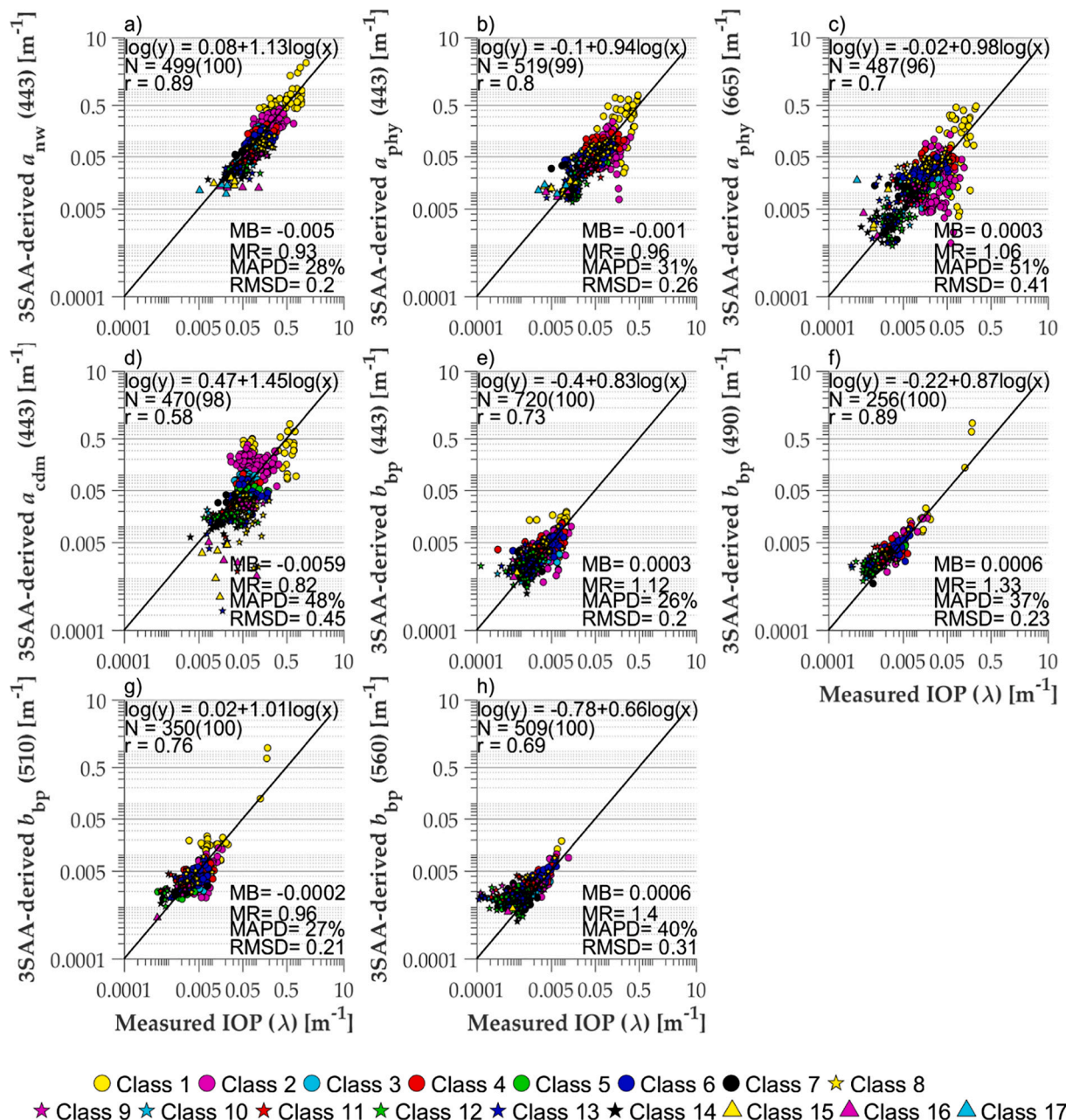


Fig. 10. Same as Fig. 7 but for DS-Sat. The different colors and symbols represent the different OWCs.

b_{bp} at 443 nm are 28% (-0.005 m^{-1}), 31% (-0.001 m^{-1}), 48% (-0.0059 m^{-1}) and 26% (0.0003 m^{-1}), respectively. The MAPD and MB values for $a_{phy}(665)$ are 51% and 0.0003 m^{-1} , respectively. While a_{nw} and a_{phy} are retrieved with about the same MAPD values as with the in situ validation dataset (DS-MW, Fig. 7), the MAPD values using DS-Sat instead of DS-MW increase by a factor of 1.34 and 2.0 for a_{cdm} and b_{bp} , respectively. The bias values are remarkably low for all IOPs (about -0.005 m^{-1} for a_{nw} and a_{cdm} , and $3 \cdot 10^{-4}$ and $-1 \cdot 10^{-3} \text{ m}^{-1}$ for b_{bp} and a_{phy} , respectively). The slightly lower bias values observed for DS-Sat compared to those calculated using DS-MW are due to the predominance of oceanic clear waters in DS-Sat compared to DS-MW. Among the different match-up data points, the ones belonging to OWC 1 and 2 (i.e. present the lower retrieval accuracy), which may be explained by atmospheric corrections that are more challenging for these OWC (Jamet et al., 2011; Goyens et al., 2013). In general, b_{bp} is retrieved with a good accuracy at all wavelengths, although a saturation can be observed at 560 nm for $b_{bp}(560)$ values below 0.0005 m^{-1} . This saturation pattern in ultra-oligotrophic waters was not observed for the in situ dataset (see Fig. 7), and could be attributed to uncertainties in the $R_{rs}(\lambda)$ retrievals.

3SAA was also tested using the DS-Argo dataset which combines OLCI $R_{rs}(\lambda)$ data and in situ $b_{bp}(700)$ measurements. Because of the very low R_{rs} signal in the red part of the spectrum in oligotrophic waters, $b_{bp}(700)$ was calculated from the OLCI-derived $b_{bp}(443)$ retrievals and the estimated b_{bp} spectral slope, Y_{bbp} , assuming that $b_{bp}(\lambda)$ follows a power law spectral model (Morel and Maritorea, 2001; Reynolds et al., 2001; Stramska and Petelski, 2003; Loisel et al., 2006; Slade and Boss, 2015; Reynolds et al., 2016). Deviations from this monotonic spectral pattern have been observed in coastal waters, and was generally attributed to absorption effects and improper calibration (Slade and Boss, 2015).

Three different approaches have been examined to calculate Y_{bbp} from OLCI observations. First, because $b_{bp}(\lambda)$ is estimated independently at each wavelength from LS2, Y_{bbp} can be directly calculated from a linear regression between $\text{Log}(b_{bp}(\lambda))$ and $\text{Log}(\lambda)$, where λ is 443, 490, 510, and 560 nm. For the present dataset, this approach provides a median Y_{bbp} value of 1.24 with a coefficient of variation of 48%. Two empirical relationships between Y_{bbp} and the blue to green reflectance ratio (Lee et al., 2009) or chlorophyll concentration (Morel and Maritorea, 2001) were tested to extrapolate to 700 nm. The first of them is the parameterization of Lee et al. (2009) adopted in QAA-v6 and GIOPs default configuration (as described in Werdell et al., 2013). It provides a higher Y_{bbp} median value (1.97) with a much lower coefficient of variation (11.1%) over the present dataset (Fig. 11). This pattern is

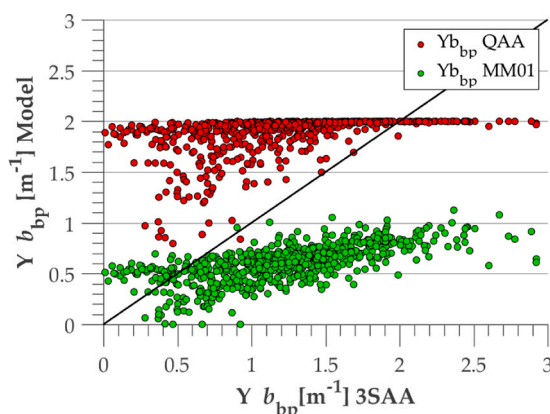


Fig. 11. Comparison of either QAA-derived (red) or Morel and Maritorea (2001) (green) derived Y_{bbp} values as a function of 3SAA-derived Y_{bbp} values for the DS-Argo dataset. The solid line is the 1:1 line. (For interpretation of the references to color in this figure legend, the reader is referred to the web version of this article.)

explained by the fact that for a blue to green reflectance ratio higher than about 4, which represents a large part of the open oceanic waters, the Y_{bbp} values estimated from QAA-v6 saturate at a value of ~ 2.0 . At last, the Chl-based parameterization of Morel and Maritorea (2001), based on theoretical considerations, provides a much lower median value (0.63) and a coefficient of variation of 32% (Fig. 11). In both cases, the retrieved Y_{bbp} is too low for oligotrophic waters (Antoine et al., 2011). The application of these three different algorithms on a monthly OLCI image (May 2018) clearly shows some spatial discrepancies between the 3 considered models (Fig. 12). While Y_{bbp} saturates over a large part of open ocean waters using band ratio relationships (Fig. 12c, d), it exhibits much lower values from the Chl-based approach (Fig. 12e, f). In situ measurements performed in two contrasted marine environments and covering oligotrophic to eutrophic waters showed a broad range of Y_{bbp} values, with values around 3 in oligotrophic waters to 0–1 in eutrophic waters (Antoine et al., 2011). This range of values is in better agreement with the Y_{bbp} values obtained from the b_{bp} regression approach (Fig. 12a,b), which was therefore selected.

The $b_{bp}(700)$ estimates derived from the 3SAA Y_{bbp} and $b_{bp}(443)$ determinations using the OLCI data show a good agreement between the model-derived and measured particulate backscattering coefficient over the entire range of observed b_{bp} values, with however a more pronounced scatter around the 1:1 line in very clear waters (Fig. 13). The MAPD, bias, and RMSD values are 30%, 0.0001 m^{-1} , and 0.22 respectively, in good agreement with the values obtained at 443 nm using DS-Sat (Fig. 10). Conserving only the data points, for which the linear regression used to retrieve Y_{bbp} from $\text{Log}(b_{bp}(\lambda))$ versus $\text{Log}(\lambda)$ has a r^2 value higher than 0.7, improves significantly the performance of the model with a MAPD value of 22.8%.

3.3. Comparison between 3SAA, GSM and QAA with the in situ datasets

The performance of the 3SAA algorithm is compared to that of QAA v6 and GSM-GC on the coastal and open waters dataset (DS-MW). This exercise is not performed for the inland water dataset as these models have only been developed for marine waters. Previous studies have indeed clearly shown the necessity to adapt QAA for inland waters (Mishra et al., 2013; Li et al., 2016; Ogashawara et al., 2016; Rodrigues et al., 2018). The results of this inter-comparison are presented at 443 nm and at 665 nm for a_{phy} . In general, the 3 algorithms show a good performance for the retrieval of all IOPs, and are able to retrieve $a_{nw}(443)$ and $b_{bp}(443)$ for all data points (1309 for $a_{nw}(443)$ and 11,292 for $b_{bp}(443)$). The number of retrievals of $a_{phy}(443)$ decreases to 94% (72 negative solutions on 1139 data points) for QAA-v6, while no negative solutions are obtained with 3SAA or GSM. For $a_{cdm}(443)$, QAA-v6 and 3SAA retrieve 10 and 18 negative values (on 1037 data points), respectively, while no negative solutions are obtained by GSM. Negative solutions are removed and considered as a model failure for this inter-comparison exercise, and the statistical indicators provided below are all calculated on the same number of data points, and for this reason, the number of valid data points is the same for the three models.

The three models present good retrieval accuracies for the different IOPs (Fig. 14), with however some slight differences as discussed below, and with the exception of $a_{phy}(665)$ for which QAA-v6 clearly fails in contrast to GSM-GC and 3SAA which present MAPD (and bias) values of 39% (-0.0017 m^{-1}) and 44% (-0.0009 m^{-1}), respectively. In contrast to QAA, and as mentioned previously, the retrieval of $a_{phy}(665)$ and $a_{phy}(443)$ are not fully independent for both 3SAA and GSM.

Among the three models, $a_{nw}(443)$ is estimated with very similar performances by 3SAA (MAPD = 23%, MB = -0.0147 m^{-1}) and QAA-v6 (MAPD = 20%, MB = -0.00878 m^{-1}), but with significantly higher MAPD (32%) and similar MB (-0.01569 m^{-1}) values for GSM-GC (Fig. 14). 3SAA and QAA-v6 show the best performance for $a_{ph}(443)$, with about the same MR and MAPD values, but with a slightly higher bias values for 3SAA (-0.004 m^{-1}) than for QAA-v6 (-0.003 m^{-1}). A slightly better retrieval accuracy of $a_{cdm}(443)$ is achieved by QAA-v6

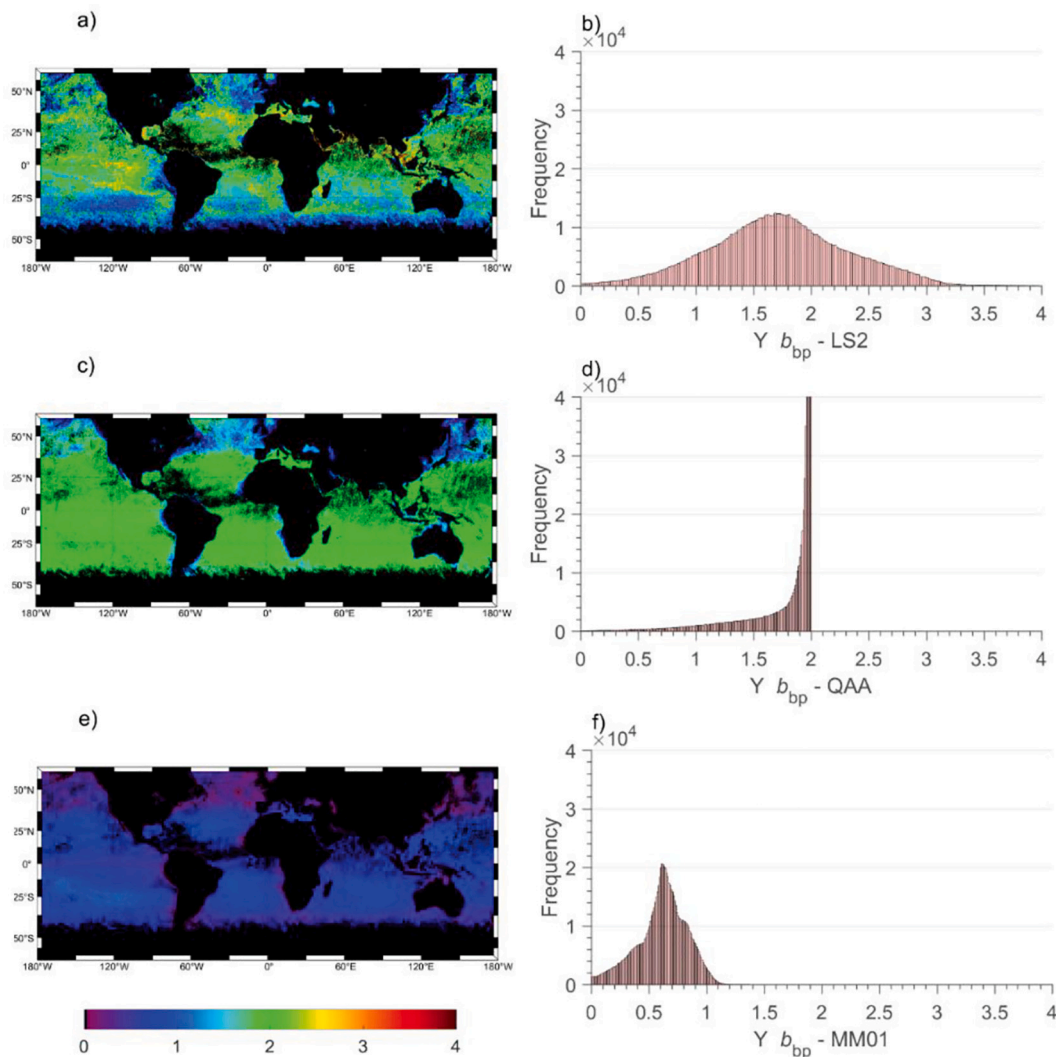


Fig. 12. Global distribution of Y_{bbp} (left column) and its corresponding histogram (right column) estimated from 3SAA, QAAv6 (Lee et al., 2009), and Morel and Maritorena (2001). In this latter algorithm, Chl-a is the standard OLCI product provided by the OC4Me algorithm (Morel et al., 2007).

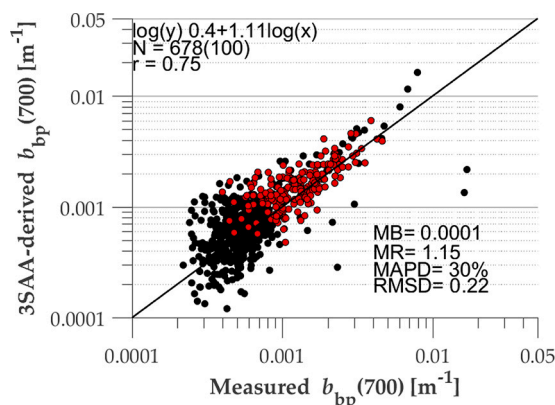


Fig. 13. Comparison of LS2-derived and measured values of $b_{bp}(700)$ for the DS-Argo dataset. The different statistical indicators calculated for the data of LS2-derived versus measured $b_{bp}(700)$ are provided (see text for details). The solid line is the 1:1 line. The circles in red correspond to the stations for which the linear regression used to retrieve Y_{bbp} from $\text{Log}(b_{bp}(\lambda))$ versus $\text{Log}(\lambda)$ has a r^2 value higher than 0.7. (For interpretation of the references to color in this figure legend, the reader is referred to the web version of this article.)

(MAPD = 28% and MB = -0.004 m^{-1}) while both 3SAA and GSM-GC present slightly higher MAPD values (33%), and bias (about -0.01 m^{-1}). The best retrieval accuracy for $b_{bp}(443)$ is obtained with 3SAA (MAPD = 13% and MB = 0.00014 m^{-1}), with a MB and MAPD values roughly two times higher for GSM-GC reflecting the large scatter around the 1:1 line observed for very clear waters. Overall, for all three models the retrieval accuracy was higher for b_{bp} , than a_{nw} , a_{cdm} and a_{phy} , consistently with the results of other studies presenting IOP retrieval and apportioning methods (e.g. Werdell et al., 2013; Brando et al., 2012) and with the sensitivity analysis carried out by Lee et al., 2010.

3.4. Application to remote sensing data

Finally, 3SAA is applied to the Level-3 monthly binned $R_{rs}(\lambda)$ data at 4 km spatial resolution collected by the OLCI sensor in May 2018. To reduce redundancy in the discussion, and because it is not the purpose of the present paper to perform an extensive inter-comparison exercise between the different existing inverse models, the 3SAA results were only compared with those obtained by the GSM-GC algorithm as implemented in GLOBColour (except for b_{bp} , where QAA-v6 results are also provided). As already noted in Werdell et al. (2013) for all IOPS, and recently by Bisson et al. (2019) for b_{bp} , there is an excellent agreement between QAA and GIOP, probably due to the use of the same Y_{bbp} and Y_{cdm} spectral slopes in the two algorithms. Note that relatively

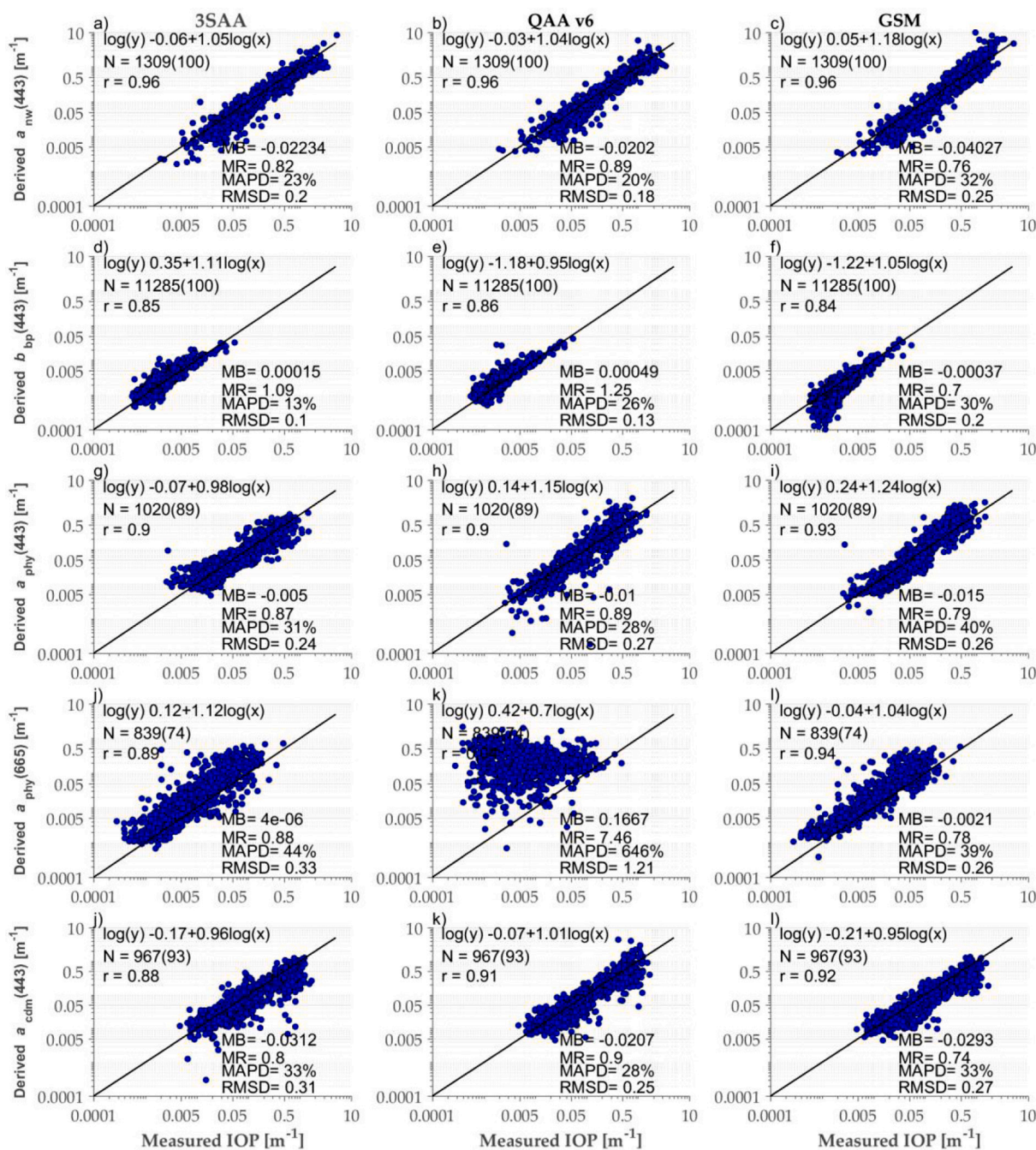


Fig. 14. Comparison of modeled-derived and measured values of IOPs for the DS-MW dataset. The results for the 3SAA, QAA-v6, and GSM models are provided in the left, middle, and right columns, respectively. The different statistical indicators calculated for the model-derived versus measured IOPs are provided (see text for details). The solid line is the 1:1 line.

similar retrieval patterns are generally obtained between QAA and GSM in agreement with results presented in Fig. 14 from in situ measurements, as well as from Werdell et al. (2013) from MODIS observations, especially for $a_{phy}(443)$ and $a_{cdm}(443)$. To perform this inter-comparison exercise in the same conditions, the Raman correction developed in 3SAA was not applied in any of the three models.

Well-known IOPs spatial patterns were found that agree well with previous studies (Siegel et al., 2005; Vantrepotte et al., 2012; Werdell et al., 2013). An example of global spatial distribution is provided for $b_{bp}(443)$ and compared to the results obtained from QAA-v6 (Fig. 15). An excellent agreement is found between these two products (Fig. 15d), except in South Pacific Gyre where QAA-v6 provides slightly higher values than 3SAA (Fig. 15c).

The variability of each IOPs estimated from 3SAA is consistent with expectations and with the DS-MW validation dataset used in the present study for marine waters. The geometrical mean IOP values, calculated over the global dataset (assuming a log normal distribution), are remarkably similar for 3SAA and GSM-GC: about 0.022 m^{-1} , 0.012 m^{-1} , 0.01 m^{-1} , and 0.00145 m^{-1} for $a_{nw}(443)$, $a_{cdm}(443)$, $a_{phy}(443)$, and $b_{bp}(443)$, respectively. The values of $b_{bp}(443)$ and $a_{phy}(443)$ are very close to those calculated from the Chl-based empirical relationships established by Antoine et al. (2011) ($= 0.0014 \text{ m}^{-1}$) and Bricaud et al. (1998) ($= 0.014 \text{ m}^{-1}$), respectively, using a mean Chl value of 0.23 mg. m^{-3} obtained from the same image. The global similarity between 3SAA and GSM-GC is reflected into the low averaged MAPD values calculated between these two models: 7%, 20%, 20%, and 13% for $a_{nw}(443)$,

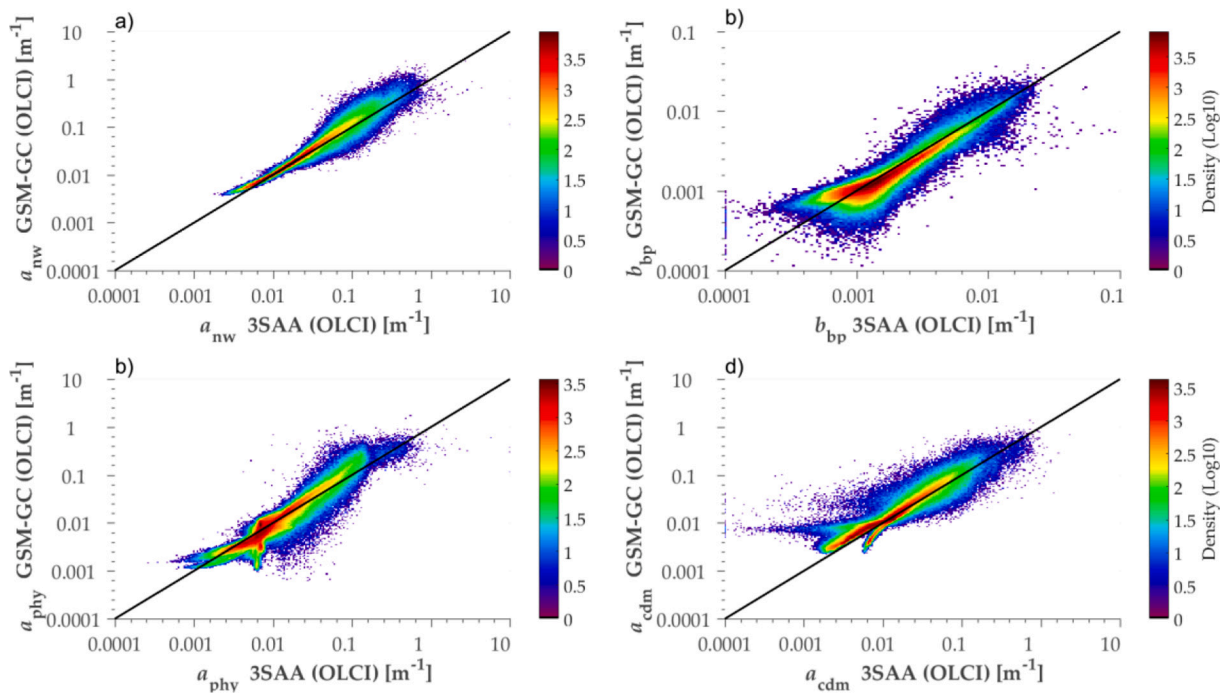


Fig. 15. May 2018 monthly comparison (density plot) for (a) a_{nw} , (b) b_{bp} , (c) a_{cdm} and (d) a_{phy} at 443 nm estimated from 3SAA and GSM-OC. The solid line is the 1:1 line.

$a_{cdm}(443)$, $a_{phy}(443)$, and $b_{bp}(443)$, respectively.

Although very similar patterns are observed in the maps generated by the two models, some significant discrepancies can be noticed. For instance, 3SAA provides lower $b_{bp}(443)$ values in gyres, and higher ones in tropical Atlantic and Indian oceans. For low $b_{bp}(443)$ values, GSM-GC

tends to return nearly constant values, explaining the horizontal segment observed around $0.0008 m^{-1}$ (6b), and the higher $b_{bp}(443)$ values retrieved by this model in gyres. This pattern, also observed for QAA-v6 but to a lower extent (Fig. 15), may be explained by the impact of Y_{bbp} in the $b_{bp}(443)$ retrieval procedure. This pattern was first

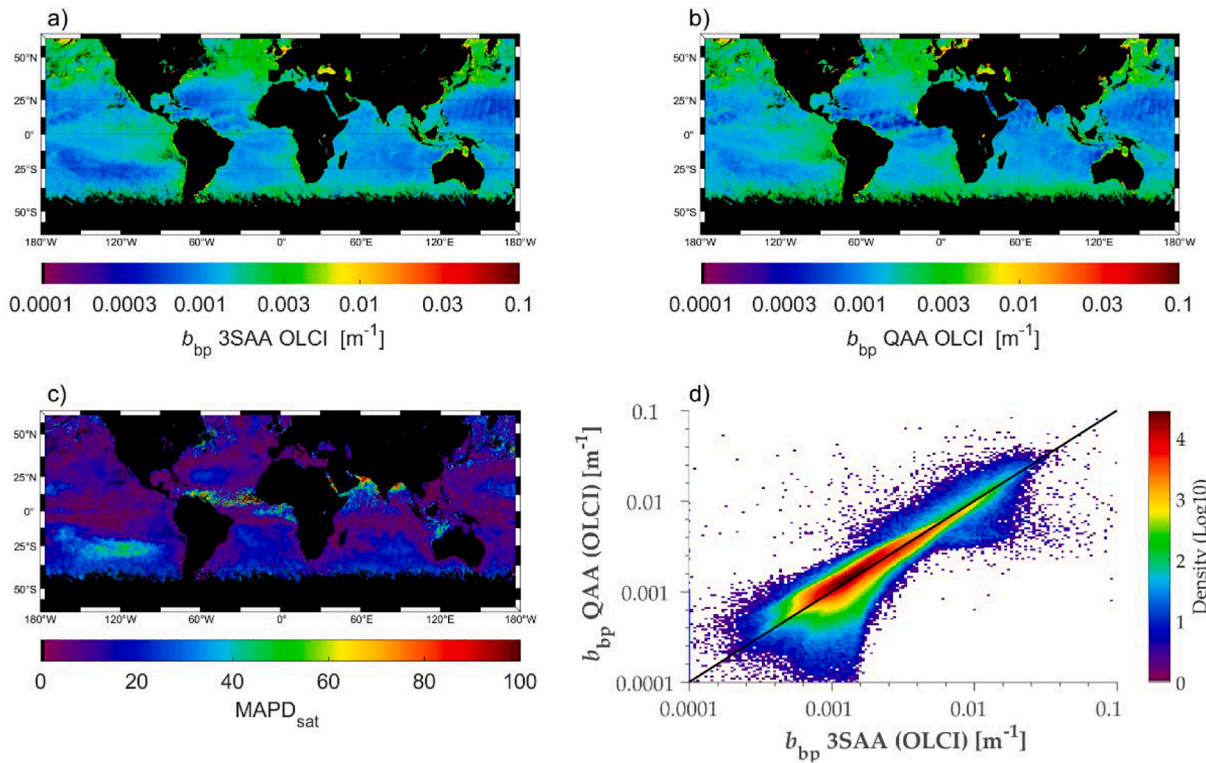


Fig. 16. May 2018 monthly OLCI composite for $b_{bp}(443)$ estimated from (a) 3SAA and (b) QAA-v6. (c) MAPD is here calculated as $200|b_{bp,QAA-v6}-b_{bp,3SAA}|/(b_{bp,QAA-v6} + b_{bp,3SAA})$. (d) Comparison (density plot) of $b_{bp}(443)$ estimated by QAA-v6 as a function of $b_{bp}(443)$ estimated by 3SAA for the OLCI image. The solid line is the 1:1 line.

observed by [Huot et al. \(2008\)](#), in which a saturation was found in b_{bp} , estimated by GSM for samples, for in situ Chl-a concentration below $0.1 \text{ mg}\cdot\text{m}^{-3}$. Meanwhile for QAA, the saturation was observed for Chl-a below $0.02 \text{ mg}\cdot\text{m}^{-3}$.

The better agreement between 3SAA and QAA-v6 compared to 3SAA and GSM-GC may be due to the adoption of a constant Y_{bbp} value (1.034) in the later model. Although [Werdell et al. \(2013\)](#) showed, through an error propagation exercise in the GIOP algorithm, that the impact of Y_{bbp} in the IOP retrieval is relatively low, the authors used an uncertainty of 33% which is probably not well adapted (see [Fig. 12](#)). Additional work should however be performed to better analyze the impact of Y_{bbp} on IOPs retrieval.

The best agreement between the two models is found for $a_{nw}(443)$, with a mean MAPD value of 7% ([Fig. 16a](#)). The highest differences (30%–40%) are found in coastal areas as well as in the South Pacific gyre. For $a_{phy}(443)$ ([Fig. 16 cc](#)) and $a_{cdm}(443)$ ([Fig. 16d](#)) the largest difference between the algorithms are observed in open waters. Compared to GSM-GC, the third step of 3SAA generally tends to estimate lower $a_{phy}(443)$ values at the gyres boundaries and in the equatorial Pacific. The reverse pattern is generally observed inside the gyres where $a_{phy}(443)$ from GSM-GC present higher values. In contrast to $a_{phy}(443)$, the highest differences between the two algorithms for the estimation of $a_{cdm}(443)$ are observed inside the gyres, where 3SAA provides lower values than GSM-GC. The different patterns observed for $a_{cdm}(443)$ and $a_{phy}(443)$ at the lower range values are in agreement with the slightly higher $a_{nw}(443)$ values estimated by GSM-GC in this range.

4. Concluding remarks

The three-step inverse method (3SAA) presented in this paper aims at estimating IOPs of surface natural waters from remote sensing reflectances measured in the visible part of the spectrum. First, the diffuse attenuation coefficient of downwelling irradiance $\langle K_d(\lambda) \rangle_1$ is estimated from $R_{rs}(\lambda)$ at the different required wavelengths from a slightly improved version of the neural network algorithm used in [Loisel et al. \(2018\)](#). Then, the total absorption and backscattering coefficients are estimated from LS2 ([Loisel et al., 2018](#)). In the third and last step, the phytoplankton and colored detrital matter absorption coefficients are assessed from $a_{nw}(\lambda)$ using a modified version of [Zhang et al. \(2015\)](#) involving Optical Water Classes. Other models could however be used at the second step of 3SAA. One may also partition differently $a_{nw}(\lambda)$ into for instance $a_p(\lambda)$ ($=a_{phy}(\lambda) + a_{nap}(\lambda)$) and $a_{cdom}(\lambda)$, or use another model allowing the particulate and dissolved part of $a_{cdm}(\lambda)$ to be derived ([Stramski et al., 2019](#)).

Unlike most operational semi-analytical algorithms, LS2 is free of any spectral assumptions on total IOPs but relies on the estimation of $\langle K_d(\lambda) \rangle_1$ from $R_{rs}(\lambda)$. As already deeply discussed in [Loisel et al. \(2018\)](#) (see their [Fig. 5](#) and [Table 2](#)), no spectral bias has been identified in the estimation of $\langle K_d(\lambda) \rangle_1$. In the second step, the adaptation of the spectral constraints through the optical water classes (OWC), allows 3SAA to better perform in various marine and inland aquatic environments. Such procedure could also be adapted to other inverse models, and easily implemented in GIOP. While 3SAA, QAA, and GSM perform similarly in retrieving the different absorption coefficients in marine waters, b_{bp} is estimated with a significantly better performance by LS2. In theory, IOPs can be estimated by 3SAA at any wavelength at which $\langle K_d(\lambda) \rangle_1$ can be derived from the NN (i.e. the visible part of the spectrum). However, the retrieval of some IOPs can be very challenging in some specific spectral domain due to their different level of contribution to the $R_{rs}(\lambda)$ signal depending on λ . For instance, as already mentioned in [Loisel et al. \(2018\)](#), the direct estimation of $a_{nw}(\lambda)$ is particularly challenging in the green and red parts of the spectrum as the contribution of $a_w(\lambda)$ considerably increases with wavelength. In the same way, the present study has shown that the retrieval of $b_{bp}(\lambda)$ cannot adequately be done in the blue part of the spectrum for very absorbing waters, such as those sampled in Amazonia. Therefore, the bands at

which the IOPs can successfully to be retrieved should be adapted to the bio-optical environment considered. OWC could inform the algorithm for the selection of the most appropriate wavelengths to use in the inversion. This study has shown that standard parameterizations of the spectral slope of $b_{bp}(\lambda)$ underestimate its natural variability compared to its direct derivation from LS2. New parameterizations should then be developed and the impact of such parameterizations on the accuracy of IOP retrievals from current SAAs should be further examined.

While 3SAA has been developed for OLCI, it can also be applied to past and current multispectral ocean color missions, using the proper look-up tables and NN algorithms (used to assess $\langle K_d(\lambda) \rangle_1$ at the relevant wavelengths). Due to its inherent characteristics, 3SAA will also be usable to process data delivered from future hyperspectral missions such as the NASA Plankton, Aerosol, Cloud, ocean Ecosystem mission ([Werdell et al., 2019](#)). Nevertheless, further work is required to test the neural network algorithm used to assess $\langle K_d(\lambda) \rangle_1$ from hyperspectral data, and to properly set the spectral constraints used to partition $a_{nw}(\lambda)$ into its different sub-components.

As a final remark, the source code in Matlab can be asked directly via e-mail, and the final version, with a more user friendly interface, will be made available in the IOCCG platform. A SNAP toolbox is also available in: <https://gitlab.eumetsat.int/eumetlab/oceans/ocean-science-studies/olci-iop-processor/-/tree/master>. This software, which include the C source code, is freely available under the term of GNU GPL3 License.

Declaration of Competing Interest

The authors declare that they have no known competing financial interests or personal relationships that could have appeared to influence the work reported in this paper.

Acknowledgments

The study was funded by the European Commission's Copernicus Programme and EUMETSAT, contract number EUM/CO/17/4600001980/EJK. We would like to recognize the time and effort done to collect the in situ measurements gathered in this study, which were collected by different research groups and for different areas across the globe. The final dataset was created from the following studies/projects: NOMAD 2015**, [Valente et al. \(2016\)](#), [Loisel et al. \(2018\)](#) (PANGEA), Plumes and blooms (funded by NASA), BOUSSOLE, funded by ESA, CNRS, INSU, and IMEV, PEACETIME cruise (Julia Uitz, Emmanuel Boss & Nils Haëntjens, contribution to the "PEACETIME-OC" project funded by CNES), NASA NAAMES cruises, LIMNADES database, specifically Annelies Hommersom in Netherlands, financed by NWO/SRON Programme Bureau Space Research, Estonian data collection and analysis were funded by the Estonian Research Council grants SF01980009s11 and PRG302, Lake Superior river and estuary collected in the frame of the NSERC funding (RGPIN-2019-06070 and RGPIN-2014-03680), Lake Erie IOPs and AOPs were provided by Dr. Caren Binding of Environment and Climate Change Canada, Lake Superior described in [Mouw et al., 2017](#) and [Casey et al., 2020](#) publications and Mamiraua project in Brazil (Claudio Barbosa & Evlyn Novo), funded by FAPESP n.° 2014/23903-9, MSA-BNDES n.° 1022114003005 and CNPq n.° 461469/2014-6). The BGC-ARGO data were collected and made freely available by the International Argo Program and the national programs that contribute to it (<http://www.argo.ucsd.edu>, <http://argo.jcommops.org>). The BGC-Argo Program is part of the Global Ocean Observing System. We also thank ESA, EUMETSAT and ACRI-ST for freely processing and providing Sentinel-3 images. We would also like to thank Emmanuel Boss for the comments as part of the scientific comity member of this project and during the earlier versions of this manuscript.

References

- Antoine, D., Chami, M., Claustre, H., d'Ortenzio, F., Morel, A., Bécu, G., Gentili, B., Louis, F., Ras, J., Roussier, E., Scott, A.J., Taillez, D., Hooker, S.B., Gueval, P., Deste, J., Dempsey, C., Adams, D., 2006. BOUSSOLE: A Joint CNRS-INSU, ESA, CNES, and NASA ocean color calibration and validation activity.
- Antoine, D., Siegel, D.A., Kostadinov, T., Maritorena, S., Nelson, N.B., Gentili, B., Vellucci, V., Guillocheau, N., 2011. Variability in optical particle backscattering in contrasting bio-optical oceanic regimes. *Limnol. Oceanogr.* 56 (3), 955–973.
- Bailey, S., Wang, M., 2001. Satellite Aerosol Optical Thickness Match-up Procedures. NASA Technical Memorandum, 2001–209982 (Pp. 70–72). NASA Goddard Space Flight Center, Greenbelt, MD.
- Balazsbramanian, S.V., Pahlevan, N., Smith, B., Binding, C., Schalles, J., Loisel, H., Gurlin, D., Greb, S., Alikas, K., Randa, M., Bunkei, M., Moses, W., Nguyễn, H., Lehmann, M., O'Donnell, D., Ondrusek, P., Han, T., Fichot, C.G., Moore, T., Boss, E., 2020. Robust algorithm for estimating Total suspended solids (TSS) in inland and Nearshore coastal Waters. *Remote Sens. Environ.* 246, 111768 (ISSN 0034-4257).
- Béanger, S., Carrascal-Leal, C., Jaegler, T., Larouche, P., Galbraith, P., 2017. Assessment of radiometric data from a buoy in the St. Lawrence estuary. *J. Atmos. Ocean. Technol.* 34 (4), 877–896.
- Binding, C.E., Greenberg, T.A., McCullough, G., Watson, S.B., Page, E., 2018. An analysis of satellite-derived chlorophyll and algal bloom indices on Lake Winnipeg. *J. Great Lakes Res.* 44 (3), 436–446.
- Bisson, K.M., Boss, E., Westberry, T.K., Behrenfeld, M.J., 2019. Evaluating satellite estimates of particulate backscatter in the global open ocean using autonomous profiling floats. *Opt. Express* 27 (21), 30191–30203.
- Brando, V.E., Dekker, A.G., Park, Y.J., Schroeder, T., 2012. Adaptive semianalytical inversion of ocean color radiometry in optically complex waters. *Appl. Opt.* 51 (15), 2808–2833.
- Brewin, R.J.W., Sathyendranath, S., Müller, D., Brockmann, C., Deschamps, P.Y., Devred, E., Doerffer, R., Fomferra, N., Franz, B., Grant, M., Groom, S., Horseman, A., Hu, C., Krasemann, H., Lee, Z., Maritorena, S., Melin, F., Peter, M., Platt, T., Regner, P., Smyth, T., Steinmetz, F., Swinton, J., Werdell, J., White, G.N., 2015. The ocean colour climate change initiative: III, A round-robin comparison in in-water bio-optical algorithms. *Remote Sens. Environ.* 162, 271–294.
- Bricaud, A., Morel, A., Prieur, L., 1981. Absorption by dissolved organic matter of the sea (yellow substance) in the UV and visible domains. *Limnol. Oceanogr.* 26 (1), 43–53.
- Bricaud, A., Babin, M., Morel, A., Claustre, H., 1995. Variability in the chlorophyll-specific absorption coefficient of natural phytoplankton: analysis and parametrization. *J. Geophys. Res.* 100 (C7), 13321–13332.
- Bricaud, A., Morel, A., Babin, M., Allali, K., Claustre, H., 1998. Variations of light absorption by suspended particles with chlorophyll a concentration in oceanic (case 1) waters: analysis and implications for bio-optical models. *J. Geophys. Res. Oceans* 103 (C13), 31033–31044.
- Bricaud, A., Babin, M., Claustre, H., Ras, J., Tièche, F., 2010. Light absorption properties and absorption budget of Southeast Pacific waters. *J. Geophys. Res. Oceans* 115 (C8).
- Casey, K.A., Rousseaux, C.S., Gregg, W.W., Boss, E., Chase, A.P., Craig, S., Mouw, C.B.E., Reynolds, R.A., Stramski, D., Ackleson, S.G., Bricaud, A., Schaeffer, B., Lewis, M.R., Maritorena, S., 2020. A global compilation of in situ aquatic high spectral resolution inherent and apparent optical property data for remote sensing applications. *Earth Syst. Sci. Data* 12, 1123–1139. <https://doi.org/10.5194/essd-12-1123-2020>.
- Cetinić, I., Perry, M.J., Briggs, N.T., Kallin, E., D'Asaro, E.A., Lee, C.M., 2012. Particulate organic carbon and inherent optical properties during 2008 North Atlantic bloom experiment. *J. Geophys. Res.* 117, C06028 <https://doi.org/10.1029/2011JC007771>.
- Ciotti, A.M., Bricaud, A., 2006. Retrievals of a size parameter for phytoplankton and spectral light absorption by colored detrital matter from water-leaving radiances at SeaWiFS channels in a continental shelf region off Brazil. *Limnol. Oceanogr. Methods* 4, 237–253.
- Claustre, H., Johnson, K.S., Takeshita, Y., 2020. Observing the Global Ocean with biogeochemical-Argo. *Annu. Rev. Mar. Sci.* 12, 23–48.
- Devred, E., Sathyendranath, S., Stuart, V., Platt, T., 2011. A three component classification of phytoplankton absorption spectra: application to ocean-color data. *Remote Sens. Environ.* 115 (9), 2255–2266.
- Doerffer, R., Fischer, J., 1994. Concentrations of chlorophyll, suspended matter, and gelbstoff in case II waters derived from satellite coastal zone color scanner data with inverse modeling methods. *J. Geophys. Res. Oceans* 99 (C4), 7457–7466.
- Doerffer, R., Heymann, K., Schiller, H., 2002. Case 2 water algorithm for the medium resolution imaging spectrometer (MERIS) on ENVISAT. Proceedings of the ENVISAT Validation Workshop, 9–13 December 2002, ESA Report.
- Doxaran, D., Leymarie, E., Nechad, B., Dogliotti, A., Ruddick, K., Gernez, P., Knaeps, E., 2016. Improved correction methods for field measurements of particulate light backscattering in turbid waters. *Opt. Express* 24 (4), 3615–3637.
- Duforêt-Gaurier, L., Loisel, H., Dessailly, D., Nordkvist, K., Alvain, S., 2010. Estimates of particulate organic carbon over the euphotic depth from in situ measurements. Application to satellite data over the global ocean. *Deep Sea Res. Part I Oceanographic Res. Papers* 57 (3), 351–367.
- Ferrari, G.M., 2000. The relationship between chromophoric dissolved organic matter and dissolved organic carbon in the European Atlantic coastal area and in the West Mediterranean Sea (gulf of lions). *Mar. Chem.* 70 (4), 339–357.
- Friedrichs, M.A.M., Carr, M.-E., Barber, R.T., Scardi, M., Antoine, D., Armstrong, R.A., Asanuma, I., Behrenfeld, M.J., Buitenhuis, E.T., Chai, F., Christian, J.R., Ciotti, A.M., Doney, S.C., Dowell, M., Dunne, J., Gentili, B., Gregg, W., Hoepffner, N., Ishizaka, J., Kameda, T., Lima, I., Marra, J., Mélin, F., Moore, J.K., Morel, A., O'Malley, R.T., O'Reilly, J., Saba, V.S., Schmelz, M., Smyth, T.J., Tjiputra, J., Waters, K., Westberry, T.K., Winguth, A., 2009. Assessing the uncertainties of model estimates of primary productivity in the tropical Pacific Ocean. *J. Mar. Syst.* 76 (1–2), 113–133.
- Garver, S.A., Siegel, D.A., 1997. Inherent optical property inversion of ocean color spectra and its biogeochemical interpretation: 1. Time series from the Sargasso Sea. *J. Geophys. Res. Oceans* 102 (C8), 18607–18625.
- GlobColour, 2020. *GlobColour User Guide*. http://www.globcolour.info/CDR_Docs/GlobCOLOUR_PUG.pdf. that can be accessed from. <http://hermes.acri.fr/>.
- Gordon, H.R., 1989. Can the Lambert-beer law be applied to the diffuse attenuation coefficient of ocean water? *Limnol. Oceanogr.* 34 (8), 1389–1409.
- Goyens, C., Jamet, C., Schroeder, T., 2013. Evaluation of four atmospheric correction algorithms for MODIS-aqua images over contrasted coastal waters. *Remote Sens. Environ.* 131, 63–75.
- Huot, Y., Morel, A., Twardowski, M.S., Stramski, D., Reynolds, R.A., 2008. Particle optical backscattering along a chlorophyll gradient in the upper layer of the eastern South Pacific Ocean. *Biogeosciences* 5 (2), 495–507.
- IOCCG, 2006. Remote sensing of inherent optical properties: fundamentals, tests of algorithms, and applications. In: Lee, Z.P. (Ed.), Reports of the International Ocean-Colour Coordinating Group, No. 5. IOCCG, Dartmouth, 2006.
- Jamet, C., Loisel, H., Kuchinke, C.P., Ruddick, K., Zibordi, G., Feng, H., 2011. Comparison of three SeaWiFS atmospheric correction algorithms for turbid waters using AERONET-OC measurements. *Remote Sens. Environ.* 115 (8), 1955–1965. <https://doi.org/10.1016/j.rse.2011.03.018>.
- Jamet, C., Loisel, H., Dessailly, D., 2012. Retrieval of the spectral diffuse attenuation coefficient $K_d(\lambda)$ in open and coastal ocean waters using a neural network inversion. *J. Geophys. Res. Oceans* 117 (C10).
- Jorge, D.S.F., Barbosa, C.C., De Carvalho, L.A.S., Affonso, A.G., Lobo, F.D.L., Novo, E.M. D.M., 2017. Snr (signal-to-noise ratio) impact on water constituent retrieval from simulated images of optically complex amazon lakes. *Remote Sens.* 9 (7), 644.
- Kirk, J.T., 1984. Attenuation of solar radiation in scattering-absorbing waters: a simplified procedure for its calculation. *Appl. Opt.* 23 (21), 3737–3739.
- Kostadinov, T.S., Siegel, D.A., Maritorena, S., 2009. Retrieval of the particle size distribution from satellite ocean color observations. *J. Geophys. Res. Oceans* 114 (C9). <https://doi.org/10.1029/2009JC005303>.
- Kostadinov, T.S., Siegel, D.A., Maritorena, S., 2010. Global variability of phytoplankton functional types from space: assessment via the particle size distribution. *Biogeosciences* 7 (3), 3239–3257. <https://doi.org/10.5194/bg-7-3239-2010>.
- Kostadinov, T.S., Siegel, D.A., Maritorena, S., Guillocheau, N., 2012. Optical assessment of particle size and composition in the Santa Barbara Channel, California. *Appl. Opt.* 51 (16), 3171–3189.
- Kutser, T., Paavel, B., Verpoorter, C., Ligi, M., Soomets, T., Toming, K., Casal, G., 2016. Remote sensing of black lakes and using 810 nm reflectance peak for retrieving water quality parameters of optically complex waters. *Remote Sens.* 8 (6), 497.
- Lee, Z., Carder, K.L., Hawes, S.K., Steward, R.G., Peacock, T.G., Davis, C.O., 1994. Model for the interpretation of hyperspectral remote-sensing reflectance. *Appl. Opt.* 33 (24), 5721–5732.
- Lee, Z., Carder, K.L., Mobley, C.D., Steward, R.G., Patch, J.S., 1999. Hyperspectral remote sensing for shallow waters: 2. Deriving bottom depths and water properties by optimization. *Appl. Opt.* 38 (18), 3831–3843.
- Lee, Z., Carder, K.L., Arnone, R.A., 2002. Deriving inherent optical properties from water color: a multiband quasi-analytical algorithm for optically deep waters. *Appl. Opt.* 41 (27), 5755–5762.
- Lee, Z., Lubac, B., Werdell, J., Arnone, R., 2009. An update of the quasi-analytical algorithm (QAA-v5) (open file online at: <http://www.ioccg.org/groups/software/OCA.QAA.v5.pdf>).
- Lee, Z., Arnone, R., Hu, C., Werdell, P.J., Lubac, B., 2010. Uncertainties of optical parameters and their propagations in an analytical ocean color inversion algorithm. *Appl. Opt.* 49 (3), 369–381.
- Lee, Z., Lubac, B., Werdell, J., Arnone, R., 2014. Update of the Quasi-Analytical Algorithm (QAA v6)[R/OL]. International Ocean Color Group Software Report [2013-04-03] (http://www.ioccg.org/groups/Software-OCA/OAA_v6).
- Lee, Z., Wei, J., Voss, K., Lewis, M., Bricaud, A., Huot, Y., 2015. Hyperspectral absorption coefficient of “pure” seawater in the range of 350–550 nm inverted from remote sensing reflectance. *Applied Optics* 54 (3), 546–558.
- Li, S., Song, K., Mu, G., Zhao, Y., Ma, J., Ren, J., 2016. Evaluation of the quasi-analytical algorithm (QAA) for estimating Total absorption coefficient of turbid inland Waters in Northeast China. *IEEE J. Selected Topics in Appl. Earth Observ. Remote Sensing* 9 (9), 4022–4036.
- Loisel, H., Stramski, D., 2000. Estimation of the inherent optical properties of natural waters from the irradiance attenuation coefficient and reflectance in the presence of Raman scattering. *Appl. Opt.* 39 (18), 3001–3011.
- Loisel, H., Bosc, E., Stramski, D., Oubelkheir, K., Deschamps, P.Y., 2001. Seasonal variability of the backscattering coefficient in the Mediterranean Sea based on satellite SeaWiFS imagery. *Geophys. Res. Lett.* 28 (22), 4203–4206.
- Loisel, H., Nicolas, J.M., Deschamps, P.Y., Frouin, R., 2002. Seasonal and inter-annual variability of particulate organic matter in the global ocean. *Geophys. Res. Lett.* 29 (24), 1–49.
- Loisel, H., Nicolas, J.M., Sciandra, A., Stramski, D., Poteau, A., 2006. Spectral dependency of optical backscattering by marine particles from satellite remote sensing of the global ocean. *J. Geophys. Res. Oceans* 111 (C9).
- Loisel, H., Stramski, D., Dessailly, D., Jamet, C., Li, L., Reynolds, R.A., 2018. An inverse model for estimating the optical absorption and backscattering coefficients of seawater from remote-sensing reflectance over a broad range of oceanic and coastal marine environments. *J. Geophys. Res. Oceans* 123 (3), 2141–2171.
- Lubac, B., Loisel, H., 2007. Variability and classification of remote sensing reflectance spectra in the eastern English Channel and southern North Sea. *Remote Sens. Environ.* 110 (1), 45–58.

- Mannino, A., Russ, M.E., Hooker, S.B., 2008. Algorithm development and validation for satellite-derived distribution of DOC and CDOM in the U.S Middle Atlantic Bight. *J. Geophys. Res. Oceans* 113 (C7).
- Maritorena, S., Siegel, D.A., Peterson, A.R., 2002. Optimization of a semi-analytical ocean color model for global-scale applications. *Appl. Opt.* 41 (15), 2705–2714.
- Maritorena, S., d'Andon, O.H.F., Mangin, A., Siegel, D.A., 2010. Merged satellite ocean color data products using a bio-optical model: characteristics, benefits and issues. *Remote Sens. Environ.* 114 (8), 1791–1804.
- Mason, J.D., Cone, M.T., Fry, E.S., 2016. Ultraviolet (250–550 nm) absorption spectrum of pure water. *Appl. Opt.* 55 (25), 7163–7172.
- Mélin, F., Vantrepotte, V., 2015. How optically diverse is the coastal ocean? *Remote Sens. Environ.* 160, 235–251.
- Mishra, S., Mishra, D.R., Lee, Z., 2013. Bio-optical inversion in highly turbid and cyanobacteria-dominated waters. *IEEE Trans. Geosci. Remote Sens.* 52 (1), 375–388.
- Morel, A., Loisel, H., 1998. Apparent optical properties of oceanic water: dependence on the molecular scattering contribution. *Appl. Opt.* 37 (21), 4765–4776.
- Morel, A., Maritorena, S., 2001. Bio-optical properties of oceanic waters: a reappraisal. *J. Geophys. Res. Oceans* 106 (C4), 7163–7180.
- Morel, A., Prieur, L., 1977. Analysis of variations in ocean color I. *Limnol. Oceanogr.* 22 (4), 709–722.
- Morel, A., Huot, Y., Gentili, B., Werdell, J., Hooker, S.B., Franz, B.A., 2007. Examining the consistency of products derived from various ocean color sensors in open ocean (case 1) waters in the perspective of a multi-sensor approach. *Remote Sens. Environ.* 111 (1), 69–88.
- Mouw, C.B., Greb, S., Aurin, D., DiGiacomo, P.M., Lee, Z., Twardowski, M., Binding, C., Hu, C., Ma, R., Moore, T., Moses, W., Craig, S.E., 2015. Aquatic color radiometry remote sensing of coastal and inland waters: challenges and recommendations for future satellite missions. *Remote Sens. Environ.* 160, 15–30.
- Mouw, C.B., Giochetto, A.B., Grunert, B., Yu, A., 2017. Expanding understanding of optical variability in Lake Superior with a 4-year dataset. *Earth System Science Data* 9 (2), 497–509.
- Neukermans, G., Loisel, H., Mériaux, X., Astoreca, R., McKee, D., 2012. In situ variability of mass-specific beam attenuation and backscattering of marine particles with respect to particle size, density, and composition. *Limnol. Oceanogr.* 57 (1), 124–144.
- Ogashawara, I., Mishra, D.R., Nascimento, R.F.F., Alcântara, E.H., Kampel, M., Stech, J. L., 2016. Re-parameterization of a quasi-analytical algorithm for colored dissolved organic matter dominant inland waters. *Int. J. Appl. Earth Obs. Geoinf.* 53, 128–145.
- O'Reilly, J.E., Maritorena, S., Siegel, D.A., O'Brien, M.C., Toole, D., Mitchell, B.G., Kahru, M., Chavez, F.P., Strutton, P., Cota, G.F., Hooker, S.B., McClain, C.R., Carder, K.L., Muller-Karger, F., Harding, L., Magnuson, A., Phinney, D., Moore, G.F., Aikeen, J., Arrigo, K.R., Letelier, R., Culver, M., 2000. Ocean color chlorophyll a algorithms for SeaWiFS, OC2, and OC4: Version 4. SeaWiFS postlaunch calibration and validation analyses, Part 3, pp. 9–23.
- Pitarch, J., Bellacicco, M., Organelli, E., Volpe, G., Colella, S., Vellucci, V., Marullo, S., 2020. Retrieval of particulate backscattering using field and satellite radiometry: assessment of the QAA algorithm. *Remote Sens.* 12 (1), 77.
- Reynolds, R.A., Stramski, D., Mitchell, B.G., 2001. A chlorophyll-dependent semi-analytical reflectance model derived from field measurements of absorption and backscattering coefficients within the Southern Ocean. *J. Geophys. Res. Oceans* 106 (C4), 7125–7138.
- Reynolds, R.A., Stramski, D., Neukermans, G., 2016. Optical backscattering by particles in Arctic seawater and relationships to particle mass concentration, size distribution, and bulk composition. *Limnol. Oceanogr.* 61 (5), 1869–1890.
- Robinson, W.D., Franz, B.A., Patt, F.S., Bailey, S.W., Werdell, P.J., 2003. Masks and flags updates. In: Hooker, S.B., Firestone, E.R. (Eds.), *SeaWiFS Postlaunch Technical Report Series*, Chap.6, NASA/TM-2003-206892, vol. 22, pp. 34–40.
- Rodrigues, T., Mishra, D.R., Alcântara, E., Astuti, I., Watanabe, F., Imai, N., 2018. Estimating the optical properties of inorganic matter-dominated Oligo-to-Mesotrophic inland Waters. *Water* 10 (4), 449.
- Sander de Carvalho, L.A., Barbosa, C.C.F., Novo, E.M.L.M., Rudorff, C.M., 2015. Implications of scatter corrections for absorption measurements on optical closure of Amazon floodplain lakes using the spectral absorption and attenuation meter (AC-S-WETLabs). *Remote Sens. Environ.* 157, 123–137.
- Siegel, D.A., Maritorena, S., Nelson, N.B., Behrenfeld, M.J., McClain, C.R., 2005. Colored dissolved organic matter and its influence on the satellite-based characterization of the ocean biosphere. *Geophys. Res. Lett.* 32 (20).
- Slade, W.H., Boss, E., 2015. Spectral attenuation and backscattering as indicators of average particle size. *Appl. Opt.* 54 (24), 7264–7277.
- Smyth, T.J., Moore, G.F., Hirata, T., Aiken, J., 2006. Semi-analytical model for the derivation of ocean color inherent optical properties: description, implementation, and performance assessment. *Appl. Opt.* 45 (31), 8116–8131.
- Spyrakos, E., O'Donnell, R., Hunter, P.D., Miller, C., Scott, M., Simis, S.G.H., Neil, C., Barbosa, C.C.F., Binding, C.E., Bradt, S., Bresciani, M., Dall'Olmo, G., Giardino, C., Gitelson, A.A., Kutser, T., Li, L., Matsushita, B., Martinez-Vicente, V., Matthews, M. W., Ogashawara, I., Ruiz-Verdú, A., Schalles, J.F., Tebbs, E., Zhang, Y., Tyler, A.N., 2018. Optical types of inland and coastal waters. *Limnol. Oceanogr.* 63 (2), 846–870.
- Stow, C.A., Jolliff, J., McGillicuddy, D.J., Doney, S.C., Allen, J.I., Friedrichs, M.A.M., Rose, K.A., Wallhead, P., 2009. Skill assessment for coupled biological/ physical models of marine systems. *J. Mar. Syst.* 76 (1–2), 4–15.
- Stramska, M., Petelski, T., 2003. Observations of oceanic whitecaps in the north polar waters of the Atlantic. *J. Geophys. Res. Oceans* 108 (C3).
- Stramski, D., Reynolds, R.A., Kahru, M., Mitchell, B.G., 1999. Estimation of particulate organic carbon in the ocean from satellite remote sensing. *Science* 285 (5425), 239–242.
- Stramski, D., Li, L., Reynolds, R.A., 2019. Model for separating the contributions of non-algal particles and colored dissolved organic matter to light absorption by seawater. *Appl. Opt.* 58 (14), 3790–3806.
- Uitz, J., Huot, Y., Bruyant, F., Babin, M., Claustre, H., 2008. Relating phytoplankton photophysiological properties to community structure on large scales. *Limnol. Oceanogr.* 53 (2), 614–630.
- Valente, A., Sathyendranath, S., Brotas, V., Groom, S., Grant, M., Taberner, M., Antoine, D., Arnone, R., Balch, W.M., Barker, K., Barlow, R., Bélanger, S., Berthon, J.-F., Beşiktepe, Ş., Brando, V., Canuti, E., Chavez, F., Claustre, H., Crout, R., Frouin, R., Garcia-Soto, C., Gibb, S.W., Gould, R., Hooker, S., Kahru, M., Klein, H., Kratzer, S., Loisel, H., McKee, D., Mitchell, B.G., Moisan, T., Muller-Karger, F., O'Dowd, L., Ondrusek, M., Poulton, A.J., Repecaud, M., Smyth, T., Sosik, H.M., Twardowski, M., Voss, K., Werdell, J., Wernand, M., Zibordi, G., 2016. A compilation of global bio-optical in situ data for ocean-colour satellite applications. *Earth Syst. Sci. Data* 8, 235–252.
- Vantrepotte, V., Loisel, H., Dessailly, D., Mériaux, X., 2012. Optical classification of contrasted coastal waters. *Remote Sens. Environ.* 123, 306–323.
- Vantrepotte, V., Danhiez, F.-P., Loisel, H., Ouilhon, S., Mériaux, X., Cauvin, A., Dessailly, D., 2015. CDOM-DOC relationship in contrasted coastal waters: implication for DOC retrieval from ocean color remote sensing observation. *Opt. Express* 23 (1), 33–54.
- Werdell, P.J., Franz, B.A., Bailey, S.W., Feldman, G.C., Boss, E., Brando, V.E., Dowell, M., Hirata, T., Lavender, S.J., Lee, Z., Loisel, H., Maritorena, S., Melin, F., Moore, T.S., Smyth, T.J., Antoine, D., Devred, E., d'Andon, O.H.F., Mangin, A., 2013. Generalized Ocean color inversion model for retrieving marine inherent optical properties. *Appl. Opt.* 52 (10), 2019–2037.
- Werdell, P.J., McKinna, L.I.W., Boss, E., Ackleson, S.G., Craig, S.E., Gregg, W.W., Lee, Z., Maritorena, S., Roesler, C.S., Rousseaux, C.S., Stramski, D., Sullivan, J.M., Twardowski, M.S., Tzortziou, M., Zhang, X., 2018. An overview of approaches and challenges for retrieving marine inherent optical properties from ocean color remote sensing. *Prog. Oceanogr.* 160, 186–212.
- Werdell, P.J., Behrenfeld, M.J., Bontempi, P.S., Boss, E., Cairns, B., Davis, G.T., Franz, B. A., Gliese, U.B., Gorman, E.T., Hasekamp, O., Knobelspiess, K.D., Mannino, A., Martins, J.V., McClain, C.R., Meister, G., Remer, L.A., 2019. The plankton, aerosol, cloud, ocean ecosystem (PACE) mission: status, science, advances. *Bull. Am. Meteorol. Soc.* 100 (9), 1775–1794.
- Zhang, T., Fell, F., 2007. An empirical algorithm for determining the diffuse attenuation coefficient K_d in clear and turbid waters from spectral remote sensing reflectance. *Limnol. Oceanogr. Methods* 5, 457–462.
- Zhang, X., Hu, L., He, M.-X., 2009. Scattering by pure seawater: effect of salinity. *Opt. Express* 17 (7), 5698–5710.
- Zhang, X., Huot, Y., Bricaud, A., Sosik, H.M., 2015. Inversion of spectral absorption coefficients to infer phytoplankton size classes, chlorophyll concentration, and detrital matter. *Appl. Opt.* 54 (18), 5805–5816.
- Zheng, G., Stramski, D., 2013. A model based on stacked-constraints approach for partitioning the light absorption coefficient of seawater into phytoplankton and non-phytoplankton components. *J. Geophys. Res. Oceans* 118 (4), 2155–2174.